

ASSESSMENT OF A TREATMENT PLANNING
PROTOCOL FOR THE REDUCTION OF DOSIMETRY
CALCULATION ERRORS IN RADIOTHERAPY FOR
HEAD AND NECK PATIENTS WITH DENTAL
IMPLANTS

ASSESSMENT OF A TREATMENT PLANNING
PROTOCOL FOR THE REDUCTION OF DOSIMETRY
CALCULATION ERRORS IN RADIOTHERAPY FOR
HEAD AND NECK PATIENTS WITH DENTAL
IMPLANTS

BY MOESHA EMBERRU, B.SC.

A Thesis Submitted to the School of Graduate Studies in Partial Fulfillment of the
Requirements for the Degree Master of Medical Physics

McMaster University
MASTER OF SCIENCE (2021)
Hamilton, Ontario, Canada (Radiation Sciences -Medical Physics)

TITLE: Assessment of Treatment Planning Protocol for The Reduction of
Dosimetry Calculation Errors in Radiotherapy for Head and Neck Patients with
Dental Implants.

AUTHOR: Moesha Emberru, B.Sc. (University of the West Indies)

SUPERVISOR: Dr. Orest Ostapiak

NUMBER OF PAGES: xvii, 79

ABSTRACT

Concerns arise in radiation therapy for head and neck cancers when dental prostheses are involved. These prostheses are high-density materials that induce image artifacts in computed tomography (CT) scans used for dose calculation. Two approaches are utilized in mitigating the impact of these artifacts on the accuracy of dose calculation. First, metal artifact reduction (MAR) algorithms or dual-energy CT scans are used to recover image quality. Second, a planning protocol is adopted whereby residual artifacts are manually contoured and assigned appropriate densities. This study evaluated the current planning process using a holistic approach. In this work, an axial section of a head phantom containing dental implants at the level of the oral cavity was constructed and scanned using various protocols on two different commercial scanners; Philips and Siemens, to assess the appearance of artifacts. An MVCT image set was merged with the corresponding kVCT image to improve visualization of the dental implants for use in density overrides. Three ion chamber measurement points in the simulated mouth facilitated the determination of measured dose which was compared to calculated dose at various single beam irradiation geometries. The influence of density override values on agreement between calculation and measurement was investigated for each geometry and imaging modality. Percent error was computed, and initial results compared to results manipulated by use of; a CT density table

(Head); density overrides of walls and wax; and density overrides of walls, wax, and effective density of saturation regions.

The study established that normal tissue doses are not significantly affected by metal artifact reduction (MAR) algorithms, and improvements in dose calculation compared to uncorrected CT images are small. Furthermore, the inclusion of a MVCT image set improved implant visualization reducing the treatment planning time while providing more information. Evidence led to the deduction that manual overrides of effective density for clipped OMAR CT pixels reduce dose calculation errors. When the phantom was configured with amalgam and Co-Cr-Mo alloy dental implants the effective density of these implants was found to be 4.5 g/cm³. When the phantom was configured with implants containing amalgam and gold, the effective density of amalgam in the presence of gold was 5.5 g/cm³ while gold had an effective density of 6.5 g/cm³.

The median and maximum range of errors for the uncorrected images were $\pm 0.6\%$ and 7.4% respectively for the phantom configured with amalgam and Co-Cr-Mo (tray one) and $\pm 0.5\%$ and 18.1% respectively for the phantom containing amalgam and gold (tray two). The median and maximum range of errors for the corrected images after applying overrides of effective densities were $\pm 0.5\%$ and 4.7% respectively for tray one and $\pm 0.3\%$ and 7.7% respectively for tray two. In conclusion, introduction of density overrides of walls, wax and effective density of high-density materials can reduce the errors induced by metal artifacts and improve

the accuracy of dose calculations in treatment planning systems to deliver the relevant dose to a target organ.

ACKNOWLEDGEMENTS

I express my sincere gratitude to Dr. Orest Ostapiak, my supervisor for his invaluable knowledge, support, and guidance in this research. I hope to emulate his work ethics and abilities in my forthcoming career. I thank Dr. Roxanna Vlad, Dr. Marcin Wierzbicki's and Dr. Janos Juhasz for being on my committee.

I extend my appreciation to all those in the Juravinski Cancer Center who helped me overcome all the obstacles and other research problems I encountered throughout my time. I have learned a lot of invaluable information. I also thank Dr. Laura Adams for generously providing the dental implant samples and Dr. Lesley Buckley, for her help in transporting and imaging my phantom.

I am grateful to the friends that I made over the course of my time at McMaster that helped to break the monotony of Covid-19 when possible. I would also like to thank my friends and family at home for their constant love and support throughout the last two years, I do not know how I would have made it without them.

TABLE OF CONTENTS

ABSTRACT	iii
ACKNOWLEDGEMENTS	vi
 <i>CHAPTER 1</i>	
INTRODUCTION	1
1.0.2 Metal Artifacts	2
1.0.3 Corrections of Metal Artifacts	5
1.0.4 Megavoltage Computed Tomography (MVCT)	8
1.0.5 Physics Mode: CT Number and Density	9
1.0.6 Radiotherapy Treatment Planning	11
1.0.7 Motivation.....	13
 <i>CHAPTER 2</i>	
<i>MATERIALS AND METHOD</i>	17
2.0.1 Phantom	17
2.0.2 Computed Tomography (CT) Imaging	19
2.0.3 MVCT Imaging.....	21
2.0.4 Manual Artifact Correction.....	22
2.0.5 Treatment Planning.....	24
 <i>CHAPTER 3</i>	
<i>EXPERIMENTAL MEASUREMENTS</i>	27

3.0.1 In-phantom Measurements.....	27
3.0.2 Measured Absolute Dose	29
3.0.3 Percent Dose Error	31
<i>CHAPTER 4</i>	
<i>RESULTS AND DISCUSSION</i>	34
4.0.1 Initial Results	34
4.0.2 CT to Density Table.....	47
4.0.3 Contours (Walls and Wax).....	49
4.0.4 Effective Density Determination	54
4.0.5 Final Results.....	62
<i>CHAPTER 5</i>	
CONCLUSION.....	67
5.0.2 Limitations	68
5.0.4 Considerations.....	69
5.0.3 Moving Forward	69
5.0.4 Conclusion	71
<i>BIBLIOGRAPHY</i>	73
<i>APPENDIX A</i>	
Appendix A.1: Tray one, Additional Results After Density Overrides in the Contours.....	76
Appendix A.2: Tray two, Additional Results After Density Overrides in the Contours.....	77

Appendix A.3: Tray one, Additional Results After Density Overrides of Effective Density	78
Appendix A.4: Tray two, Additional Results After Density Overrides of Effective Density	79

LIST OF FIGURES

1.0.1: Illustration of the a) Photoelectric effect and b) Compton Scatter. ⁷	4
1.0.2: a) Axial and b) sagittal CT image showing streaking artifacts, saturated pixel regions and dark bands.....	5
1.0.3: a) Simple depiction of the theoretical basics of projection-based MAR algorithms with the images on the left and their sinograms on the right. b) Sinogram showing each row is a projection along the corresponding angle on the horizontal axis. ⁷	6
Figure 1.0.4: Types of dual-energy CT systems. a) Dual-source CT scans have two x-ray tubes and two detector chains that separately capture the low- and high-energy spectra. b) Single source CT scanner with a split filter at the output of the x-ray tube, which splits the x-ray beam in the z-direction into low- and high-energy x-ray spectra. ⁷	8
1.0.5: Comparison of A) kVCT and B) hybrid kVCT/MVCT image sets. ⁷	9
1.0.6: Recommended physical density overrides for common materials.	12
1.0.7: Illustration of Treatment planning starting from simulations to the start of treatment. ²⁵	13
2.0.1: a) Axial, b) sagittal, and coronal CT scan of a head and neck patient.....	17
2.0.2: Illustration of dental tray in Autodesk Inventor equipped with ionization chamber inserts.....	18
2.0.3: A) Interchangeable tray one and B) tray two, containing chamber inserts, dental implants, wax. C) Shows implants covered with wax with positions 1-3 indicated and the D) Head phantom mounted on a stand.	19
2.0.4: Same CT-slice with artifacts due to dental prostheses in tray one using a) CT2-OMAR, b) CT3-IMAR and c) CT3-140 KV.	21
2.0.5: Comparison of dental artifacts in tray one between a) kVCT (grayscale) and b) MVCBCT (inverse grayscale) image sets.	22

2.0.6: Comparison of a) uncorrected image and b) image with contours of walls, wax and density overrides of dental overrides of implants. Image (b) also shows positions 1-3 and the isocentre (red circle) for the gantry at 0° and 180° outlined and labelled. Image c) shows the isocentre (blue outline) for the gantry angles excluding 0° and 180°.....	26
2.0.7: Illustrations showing a) the digitally reconstructed radiograph (DRR) of the phantom in a beam's eye view for gantry angle 0°. An isocenter is displayed as a sphere in blue, and dental implants are shown in red and green, respectively, b) irradiation geometry parameters linking the source and target(phantom) for gantry angles 0, 90, 195, 315.....	26
3.0.1: Phantom set up on the treatment couch with the a) ion chamber in position 1 with the cable leading to the electrometer outside the treatment room and the b) phantom undergoing irradiation at a gantry angle of 315 degrees..	27
3.0.2: a) Illustration showing irradiation parameters from a view of the treatment room and a b) three-dimensional room's eye view of the set up for the gantry at 0°, in the TPS.	29
3.0.3: Sagittal CT image of A) tray one showing the effective point of measurement at 2 cm (purple) and 2.3 cm (green) for POI_1 and of B) tray two with the effective point of measurement at 2 cm (purple).	32
4.0.1: Same CT-slice with artifacts for tray one categorized by MAR reconstructed images a) CT2-OMAR, b) CT3-IMAR, c) CT3-140 KV IMAR, and the uncorrected images d) CT2- NO OMAR and e) CT3- NO IMAR data sets.	34
4.0.2: Data collected from the CT2-OMAR, tray 2 reconstruction image set, at a gantry angle of 0° using the CT to Density Table 'JCC_Avg_Mar_09'. Graphs show A) Comparison between the TPS's clipped CT number and the extrapolated CT number corresponding to a known density of 8g/cm ³ for amalgam, labelled in red and B) Calculated dose and measured dose at	

detector positions 1-3. Error bars for measured dose are smaller than symbol size.....	36
4.0.3: Data collected from the CT2 -OMAR, tray two reconstruction image set, at gantry angle 180 ⁰ using the CT to Density Table 'JCC_Avg_Mar_09'. Graphs show A) Comparison between the TPS's CT number and the actual CT number of the sample (known density of 8 g/cm ³) and wax (known density of 0.92 g/cm ³) and the B) calculated dose and measured dose at detector positions 1-3. Error bars for measured dose are smaller than symbol size.....	37
4.0.4: Comparison of percent error for various modalities and contrast of the data between trays one and two at the axial CT slice shown at gantry angle 0 ⁰ . Tray one contains amalgam and an assumed Co-Cr-Mo alloy, while tray two has amalgam and gold materials. The axial OMAR reconstructed CT image with overlaid isodose lines is shown for tray one (A) and tray two (B) tray two illustrates the distribution of the absolute dose to the three detector positions using coloured isodose lines. (C) The beam angles are shown, with zero degrees (red lines) entering the mouth. Contrast of the various modalities were performed for tray one (D) and tray two (E) with the detector positions labelled by shape. Note that CT3-140 KV is a MAR reconstructed image set.	38
4.0.5: CT number as a function of depth in the TPS for the two image sets, CT3-IMAR and CT3-NO IMAR, for tray one at an angle of zero degrees. Depth is measured in the direction of the beam angle (front of the mouth to the center of the head). Positions 1-3 are labelled.	40
4.0.6: CT number as a function of depth in the TPS for the two image sets, CT2-OMAR, trays one and two at an angle of 0 ⁰ . Depth is measured in the direction of the beam angle (front of the mouth to the center of the head). Positions 1-3 are labelled.	41

4.0.7: The images in the left column are Axial OMAR reconstructed CT images for tray one at various gantry angles with detector positions shown and coloured absolute isodose lines overlaid. The plots in the right column are the corresponding percent error by imaging modality for tray two consisting of Amalgam and Gold at various gantry angles. Shapes indicate positions 1-3. Note that readings were taken at 2cm from the base of the phantom in the region consisting of significant artifacts. (A & B) Gantry at 180⁰; (C & D) gantry at 45⁰; (E & F) gantry at 135⁰; (G & H) gantry at 90⁰. Note that CT3-140 KV is a MAR reconstructed image set..... 42

4.0.8: CT number as a function of depth in the TPS for the two image sets, CT3-IMAR and CT3-NO IMAR, for tray two at an angle of 45⁰. Depth is measured in the direction of the beam angle. Position one is labelled. 44

4.0.9: Distribution of Percent Error as a function of detector position for trays one and two, presented over all modalities and angles. For tray one, measurements were taken at 2cm and 2.3cm from the base of the phantom. Measurements for tray 2 were also taken at 2cm. Note that CT3-140 KV is a MAR reconstructed image set. 45

4.0.10: Distribution of Percent Error over all positions and angles related to modality for trays, one and two. For tray one, measurements were taken at 2cm and 2.3cm from the base of the phantom. 46

4.0.11: CT # to Density plots available for use within the TPS. The Reference table, 'JCC_Avg_Mar_09', is used clinically for all planned patients (Juravinski Cancer Centre, 2021). 47

4.0.12: Distribution of percent error for all positions and angles related to modality for trays, one and two. The right plot represents calculations taken using the CT to Density table 'JCC_Avg_Mar_09'. The left plot represents calculations using the CT to Density tables measured using the head geometry.....48

4.0.13: Comparison of percent error between the Reference CT to Density Table and CT to Density (Head geometry) for position one of tray two, for all angles.....	49
4.0.14: Image of the axial OMAR reconstructed CT image for tray one. The image on the left has (A) has no density overrides, whereas the image on the right (B) has manual density overrides corresponding to the walls and wax. ...	50
4.0.15: Percent error distributed for all positions and angles as related to modality for trays, one and two. The left plot shows data from an original scan with MAR correction, while the right plot shows the spread of percent error after applying density overrides for wax and walls.....	51
4.0.16: Percent error plotted as a function of modality for tray one and two for the gantry at 0° and 180° . Shapes indicate positions 1-3. Categories are denoted by colour. Note that readings were taken at 2cm from the base of the phantom in the region consisting of major artifacts from both trays.	52
4.0.17: Percent error as a function of modality for trays one and two for gantry at 45° and 135° . Shapes indicate positions 1-3. Categories are denoted by colour. Note that readings were taken at 2cm from the base of the phantom in the region consisting of major artifacts for both trays.	54
4.0.18: Image shows axial OMAR reconstructed CT image for (A) tray one with the addition of manual density overrides of walls and wax and the B) further addition of manual density overrides of effective density.	55
4.0.19: Percent error plotted as a function of modality for tray two with the gantry at 0° , for positions, 1 and 2. Categories are indicated by colour with five distinctions; original data (blue), data after density overrides of walls and wax (yellow), density overrides of walls, wax, and physical density (navy blue), and density overrides of walls, wax, and calculated density (red) and density of walls, wax, and low density (mustard).....	58
4.0.20: Percent error plotted as a function of modality for tray two at A) beam angle 0° , for position 1, B) beam angle 0° , for position 2, C) beam angle 45° , at	

position 3, D) angle 135 ⁰ , at position 1, E) angle 90 ⁰ , at position 2 and F) angle 270 ⁰ , for position 2. Categories are indicated by colour with six distinctions; original data (blue), data after overrides of walls and wax (yellow), density overrides of walls, wax, and physical density (navy blue), density overrides of walls, wax, and calculated density (red) and density overrides of walls, wax, and low density (mustard) and density overrides of walls, wax, and effective density (grey).....	59
4.0.21: Percent error plotted as a function of modality for tray two with the gantry at 180 ⁰ for position 1. The graph shows that changes in density overrides; Physical_Density, Calc_Density, Low_Density and Effective_Density, have a negligible effect on dose calculations. Contours_Applied, Physical_Density, Calc_Density, Low_Density and Effective_Density overlap as percent error does not change, hence, only Effective_Density is visible.....	60
4.0.22: Percent error plotted as a function of modality for tray one at beam angles 0 and 180, for position 1. Categories are indicated by colour with six distinctions; original data (blue), data after density overrides of walls and wax (yellow), density overrides of walls, wax, and physical density (navy blue), density overrides of walls, wax, and calculated density (red), density overrides of walls, wax and high density (mustard) and density overrides of walls, wax, and effective density (grey)	61
4.0.23: Comparison of relative percent error for tray one when density overrides of walls and wax are used and when they are not used.	63
4.0.24: Comparison of relative percent error for tray two when density overrides of walls, wax, and effective density were used to that when they were not...	64

LIST OF TABLES

2.0.1: Physical Density of the materials used in density overrides.....	23
3.0.1: Percent dose error (%) for the various modalities of tray two consisting of teeth with amalgam and gold implants. The CT image was manually uncorrected. The phantom was irradiated with a 6 MV photon beam for the gantry at 0 ⁰	33
4.0.1: Summary of values used in density overrides of implants.	61

LIST OF ABBREVIATIONS

CT	Computed Tomography
DECT	Dual Energy Computed Tomography
EBT	External Beam Therapy
iMAR/IMAR	Iterative Metal Artifact Reduction
JCC	Juravinski Cancer Center
kVCT	KiloVoltage Computed Tomography
kVp	Peak Kilovoltage
MAR	Metal Artifact Reduction
MVCT	MegaVoltage Computed Tomography
OMAR	Orthopedic Metal Artifact Reduction
POI	Point of Interest
ROI	Region of Interest
TPS	Treatment Planning System

CHAPTER 1

INTRODUCTION

Statistics in Canada report that approximately 5,400 people have been diagnosed with head and neck (H&N) cancers every year, with men accounting for sixty-nine percent. In 2020, about 1,500 Canadians reportedly died from head and neck cancers alone, with most persons over 45 increasing chances of experiencing dental issues. Experts classify this cancer as a tumour located in the nose, mouth, or throat comprising the pharynx, larynx, tongue, tonsils, salivary glands, and esophagus [1]. Serving a population of two million in Hamilton and surrounding regions, the Juravinski Cancer Centre (JCC) accepts approximately 400-500 new patients annually. Every week specialists see about ten new referred head and neck cancer patients [2].

Practitioners may treat head and neck cancer using surgery, radiation therapy, or chemotherapy either alone or in numerous combinations depending on factors such as disease stage. External beam therapy (EBT) is used when radiation therapy is part of the treatment process. EBT is a method that aims to destroy cancer cells by subjecting the tumour to a beam of high-energy protons or x-rays beams [3]. A linear accelerator generates the radiation beam outside the patient and is targeted at the tumour site using various techniques to minimize the dose to surrounding tissue [1]. The process is made possible by employing sophisticated

treatment planning techniques that make use of high-quality volumetric images of the patient using different modalities, the most frequent being computerized tomography (CT).

A complicating issue in radiation treatment of head and neck cancer is the presence of dental restorations, implants, and dental fillings, which consist of non-removable metallic objects that create artifacts in CT scans. Dental artifacts hinder treatment planning by making it more challenging to contour the anatomy, which may be obscured. The presence of artifacts also adversely affects the dose calculation accuracy, which relies on the accurate determination of local attenuation coefficients from CT numbers [3]. Finally, tissues adjacent to high-density dental work may receive higher doses of radiation than planned due to enhanced electron scattering [4]. Consequently, there has been much development in artifact reduction algorithms, and metal artifact reduction efforts are still a topic of interest today.

1.0.2 Metal Artifacts

In computed tomography (CT), artifacts caused by metallic implants appear as dark and bright streaks on the image. Often present is Amalgam, a material used to replace a hole left by cavities and crowns used to repair a deteriorated tooth or cover an implant in place of a tooth. Amalgam and crowns are comprised of high-density materials [5]. When therapeutic x-rays pass through these high-density objects, distinctive photon interactions influence the dose distribution in the heterogeneous media depending on size and composition. CT images are reconstructed from a

million independent detector measurements, which are assumed to be consistent; therefore, any discrepancy usually reflects an error in the reconstructed image. Artifacts are any systematic inconsistency between the CT numbers in the reconstructed image and the actual attenuation coefficients of the object [6]. Artifacts may be caused by photon scattering, photon starvation, and beam hardening and appear in the image as dark regions (cupping artifact) or bright and dark streaks (streaking artifact).

Photon starvation results from substantial attenuation when imaging x-rays pass through a dense region or a long path in a high-density object. Attenuation occurs when photons in the beam get absorbed and scattered due to interactions between the x-ray photons and the material's atoms. [7]. At energies below 200 keV, the photoelectric effect and Compton scatter dominate the interactions for diagnostic imaging. Photoelectric effect is defined as the transfer of energy from an incident photon to an inner shell atomic electron, whereby the electron is ejected from the atom (Figure 1.0.1a). In Compton scattering, an incident photon hits a free or loosely bound electron and changes direction (Figure 1.0.1b) [7]. In both cases, the x-ray beam becomes significantly attenuated after passing through even tooth cavity sized regions of high atomic number material, leaving an insufficient number of photons reaching the detectors. Photon starvation usually appears as streaks along the directions of high attenuation resulting in noise which might obscure the fine detail (Figure 1.0.2) [6].

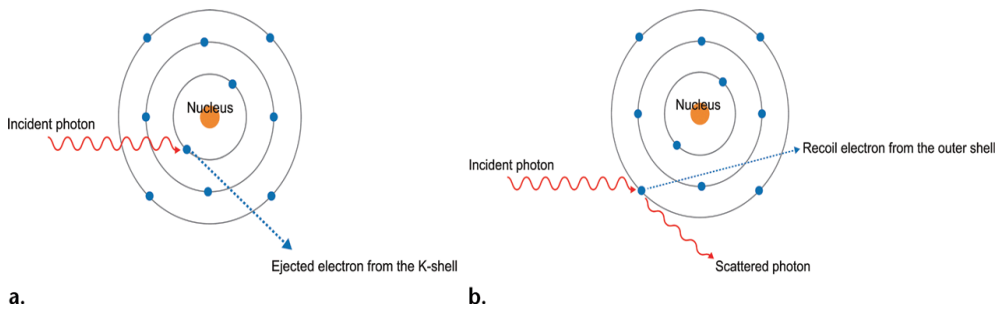
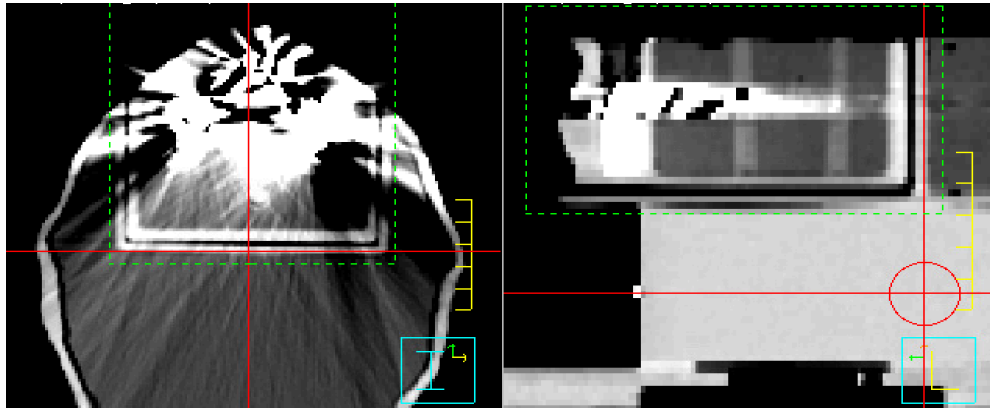


Figure 1.0.1: Illustration of the a) Photoelectric effect and b) Compton Scatter.⁷

Beam hardening is the phenomenon where an x-ray beam with a polychromatic energy spectrum passes through an object, resulting in selective attenuation of lower energy photons causing the beam to become "harder." [7] That is to say, the beam's average energy increases due to the rapid absorption of the lower energy photons compared to higher-energy photons. Cupping artifacts occur when beams that enter through the center of a uniform implant undergo more hardening than those passing through the edges as they pass through more material [6]. Dark bands and streaks appear among dense objects in heterogeneous cross-sections (Figure 1.0.2). The beam is less hardened as it passes through one of the objects at certain beam positions than when it passes through both objects at other positions [6].



a. b.
Figure 1.0.2: a) Axial and b) sagittal CT image showing streaking artifacts, saturated pixel regions and dark bands.

1.0.3 Corrections of Metal Artifacts

According to Katsura *et al.*, 2018, established solutions to photon starvation involve using higher peak voltage (kVp) settings to produce more penetrating photons that may pass through metal implants. Despite this effort, metal artifact reduction is minor, while higher peak voltage leads to a higher radiation dose to the patient. As a solution, CT vendors have developed several Metal Artifact Reduction (MAR) algorithms that work on projection data to reduce artifacts without increasing radiation dose [7]. Though there are several MAR algorithms, the following projection-based MAR algorithms used in this study are MAR for orthopedic implants (O-MAR; Philips Healthcare, Amsterdam, the Netherlands) and iterative MAR (iMAR; Siemens Healthineers, Erlangen, Germany). According to a study that evaluated the commercial techniques of different vendors, including OMAR and iMAR, algorithms do alleviate the effects of metallic objects. However, improvement depends on the details of the algorithm and the clinical situation [8].

CT images are stored and sorted as sinograms which are generated by rotating detectors around a patient and storing the detected projection profiles at each angle in the sinogram [7]. Projection-based MAR algorithms detect and segment the corrupted projection data that correspond to metallic implants. The corrupted data is then modified by substituting with approximations of the corrected values. Metal detection and segmentation is the first step in the cycle, performed using projection data (projection-based metal segmentation) or reconstructed images (image-based metal segmentation) [7]. The projection-based metal segmentation method involves directly segmenting the metal in the projection information. (Figure 1.0.3). Nevertheless, processes may vary between algorithms as major manufacturers have developed copyrighted metal artifact reduction techniques.

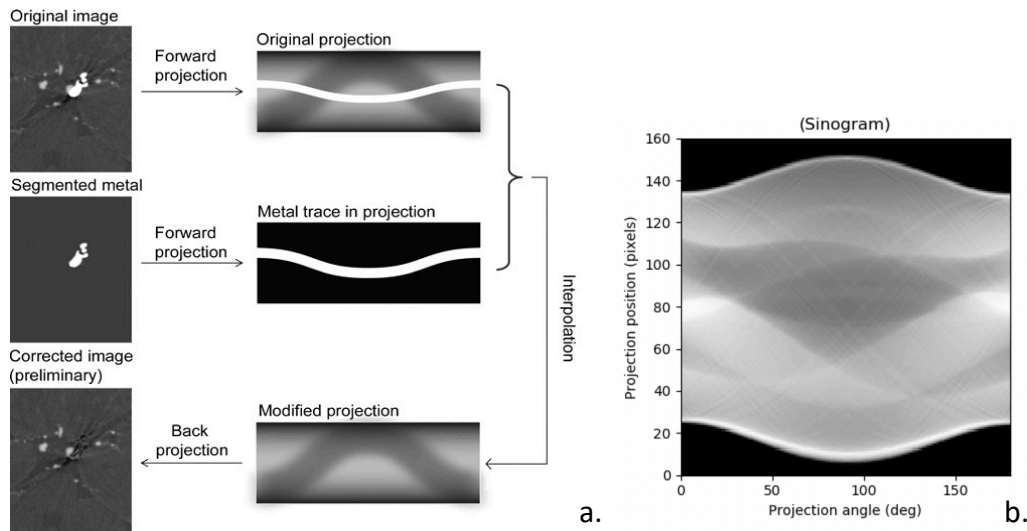


Figure 1.0.3:a) Simple depiction of the theoretical basics of projection-based MAR algorithms with the images on the left and their sinograms on the right. b) Sinogram showing each row is a projection along the corresponding angle on the horizontal axis ⁷

In addition to the MAR techniques, virtual monochromatic images generated from dual-energy (DE) CT moderates metal artifacts by reducing the effects of beam hardening. Conversely, several articles state that DECT does not often perform well as it does not address photon starvation and scatter [9] [10] [11]. Using different peak voltage energy datasets, data for two base materials (bone and soft tissue) become extrapolated, and virtual monochromatic images are synthesized [11]. The high and low tube voltage scans contain different spectral information, which, when combined, use basis material decomposition to create monochromatic images. Decomposition adjusts the weighting of the two spectra (high and low kVp) data in the reconstructed image [9]. While initial studies showed that DECT produced higher radiation dose, further investigation has shown that recently several studies have found that radiation dose from DECT is comparable to conventional SECT. This is particularly true for a technique called fast kilo-voltage switching [12].

Vendors classify dual-energy CT systems as single or dual-source CT scanners. A CT scanner with a dual-source has two x-ray tubes and two detector chains that separately produce and collect the low- and high-energy spectra (Figure 1.0.4a). A single-source CT scanner directly places a split filter at the output of the x-ray tube, splitting the low and high-energy x-ray spectra in the z-direction (Figure 1.0.4b). The DECT simulator used in this research was a single source (SOMATOM Definition AS; Siemens Healthineers) [7].

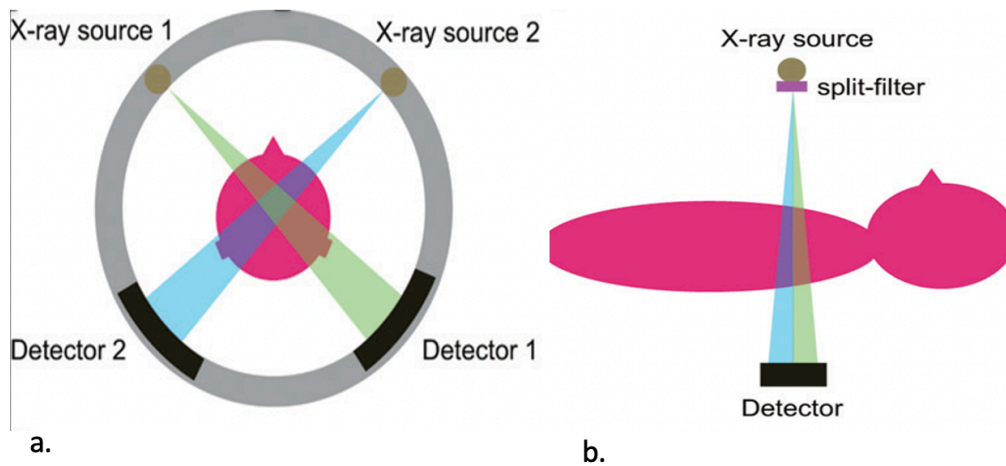


Figure 1.0.4: Types of dual-energy CT systems. (a) Dual-source CT scans have two x-ray tubes and two detector chains that separately capture the low- and high-energy spectra. (b) Single source CT scanner with a split filter at the output of the x-ray tube, which splits the x-ray beam in the z-direction into low- and high-energy x-ray spectra.⁷

1.0.4 Megavoltage Computed Tomography (MVCT)

In addition to advancements in CT reconstruction algorithms such as MAR and DECT, cone beam (MVCBCT) and fan-beam megavoltage (MVCT) images are also offered. MVCT images come directly from treatment units, and their primary use is to register patient positioning before treatment. The dose delivered to the patient is verified by recalculating the dose distribution on the MVCBCT image set produced on that day [13]. MVCBCT imaging has fewer artifacts largely due to the greater penetration of higher energy photons reducing the effect of photon starvation.

In a study, MVCT and kVCT images of a phantom that contained a hip prosthesis were compared and examined to find the effect of MVCT images on

reducing metal artifacts. Results indicated that MVCT scans allow further accuracy in CT number quantification for areas containing dental implants and regions of high-density immediately adjacent to implants [14]. In another study from London, Canada, the effects of artifacts on high-density metal hip implants for three groupings: a kVCT scan, an MVCT scan, and the creation of a hybrid image set were investigated. Findings concluded that the MVCT image provided better visualization of patient anatomy, and a hybrid kV/MVCT image allowed for the most accurate calculations (Figure 1.0.5) [15]. Findings from these studies would be considered and implemented in this thesis work.

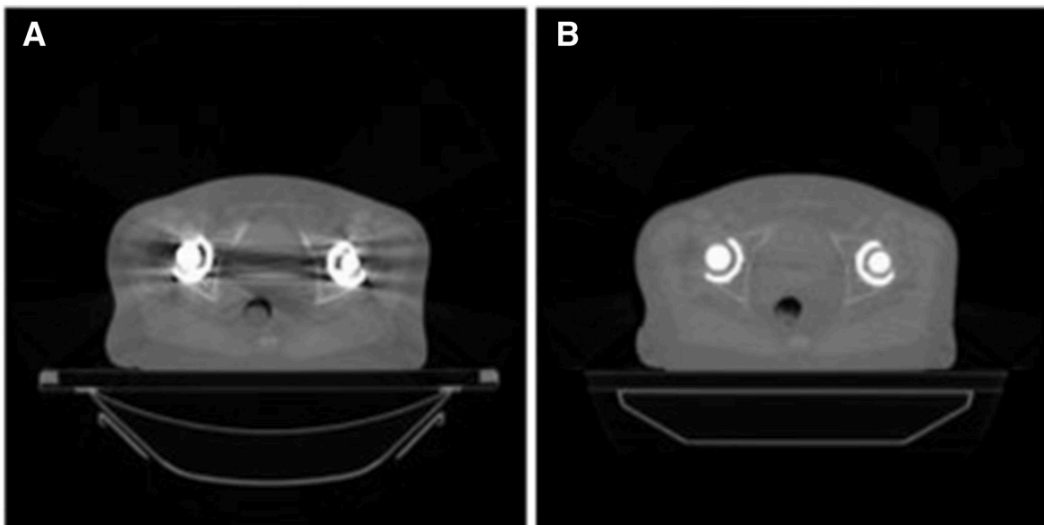


Figure 1.0.5: Comparison of A) kVCT and B) hybrid kVCT/MVCT image sets.⁷

1.0.5 Physics Mode: CT Number and Density

As discussed previously, several Metal Artifact Reduction (MAR) methods are available to improve CT image quality for radiotherapy planning and dose calculation. DECT aims to reduce the beam hardening effect while MVCT

diminishes photon starvation and noise in the image space. Despite improving volume of interest visualization and contouring (outline of organs and structures), a study in Italy observed while assessing the MAR method that these processes do not account for the metal's physical characteristics that influence dose computation in streaked regions of the CT image [16].

The Hounsfield unit (HU), also referred to as the CT number, is a relative quantitative measurement of density used to interpret computed tomography (CT) images. CT number is used because the physical density of tissue is proportional to the absorption/attenuation of an X-ray beam. The relationship is used during CT reconstruction to produce a grayscale image based on the linear transformation of the linear attenuation coefficient of the X-ray beam. In other words, the linear transformation produces a scale that displays gray tones (pixel) [17].

Hounsfield Units (HU) go from -1000 (air) to 0 (water), and 3000 for dense materials [18]. Metal implants have a CT number well beyond the 4096 limit and appear in the CT scan as regions of saturated CT number and associated artifacts. Pinnacle³ (Philips, Fitchburg, WI), planning software used through the duration of this research, maps HU to CT number ranging from 0 (air) to 1000 (water) to a limit of 4096 (just beyond dense bone). Positive values appear as bright areas representative of a region of dense tissue, i.e., more significant X-ray beam absorption, while negative values appear dark for low-density regions. Pinnacle uses a user-defined CT number to density table to translate CT number to density. Physicists create the table by taking scans of objects with known density values.

All the objects are organised in a phantom with their positions also known and the CT number recorded from the image on the scanner. The density values are related to the resultant CT values from the image. The data from the two highest density samples is linearly extrapolated beyond the upper limit of CT number of 4096 in order to assign CT numbers to regions corresponding to high density objects.

When a patient is CT scanned for planning, the CT number at each pixel is proportional to attenuation coefficient. Planning systems therefore make use of the CT number to density table to determine the physical density attributed to that pixel. Different X-ray beam energies will result in different tissue absorption and hence, different CT numbers. Levi *et al.*, 1982 examined the CT number by scanning a phantom on five CT scanners and CT to density table varied due to CT parameters such as the type of reconstructing algorithm, design of the CT, and X-ray kilovoltage [19].

1.0.6 Radiotherapy Treatment Planning

Treatment planning is the core of radiation therapy (RT) and the key to improved patient outcomes; hence effort is constantly being made to improve this process. Once the patient is scanned, and image datasets (modified by MAR algorithms or other protocols mentioned) are loaded, the radiation oncologist identifies and delineates the tumours and organs at risk (OARs) through contours [20]. Medical physicists also participate in the contouring process; one such instance is where the medical physicists may override the region of metal artifacts with density in place

of the assigned density inferred from the CT number to density table to improve the accuracy of the dosimetry calculations. The density may be smaller than the physical density of the implant as artifacts are more extensive than the actual implants. For example, at JCC, an effective density value is used for dental amalgam to override clipped OMAR CT pixels in place of the physical density of dental amalgam (Figure 1.0.6). Planning systems such as Pinnacle³ (Philips, Fitchburg, WI) are then used to develop the radiation plan.

Juravinski Cancer Center, Physics
June 8, 2016

Table of physical density overrides

Material	Physical density g/cc
Worm bridge	0.25
PLA Bolus	1.00
Soft PLA Bolus	1.12
TPU 95 Bolus	1.10
Jeltrate	1.0
Petroleum jelly gauze	0.88
Titanium	4.3
Co-Cr-Mo	7.9
Stainless Steel	8.1
Lead shield	11.3
Dental Amalgam accurately delineated	8
Dental Amalgam from clipped OMAR CT pixels	5
Gold	19.2

Figure 1.0.6: Recommended physical density overrides for common materials.

Several different radiation therapy delivery systems are available within treatment planning, but most often used for H&N cancer treatment are intensity-modulated radiotherapy (IMRT) and volumetric modulated arc therapy (VMAT). The software facilitates the optimization of dose distribution in the patient's tissue, for a given beam placement (in the case of IMRT) based on avoiding critical structures that are more sensitive to radiation. Additionally, automated

programming for multi-leaf collimator (MLC) leaf sequencing may shape the beam around critical structures during dose delivery [20].

A team comprising radiation oncologists, radiation therapists, and medical physicists/ dosimetrist then manually re-evaluates the proposed plan. They approve the type of treatment, linear accelerator beam energy, beam route, angles, and tissue contouring (Figure 1.0.7). After the treatment starts, plans may be reviewed as issues arise.

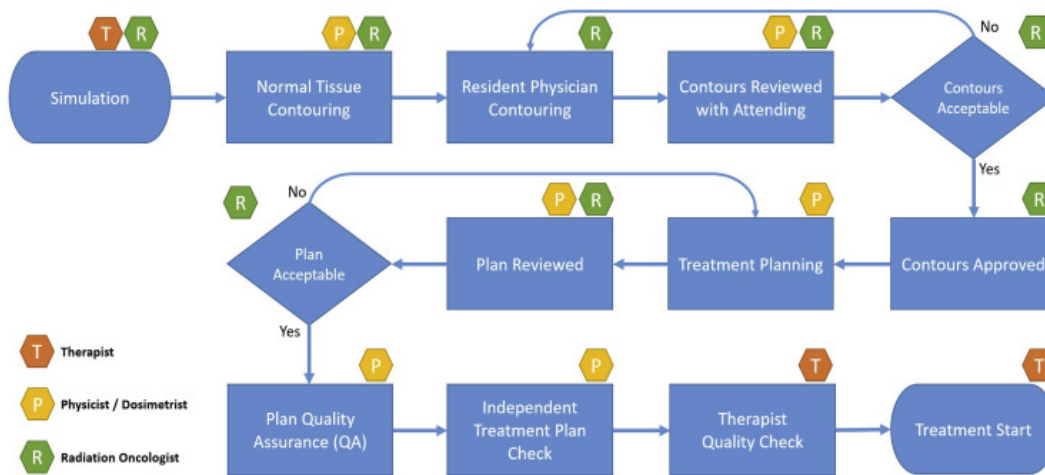


Figure 1.0.7: Illustration of Treatment planning starting from simulations to the start of treatment.²⁵

1.0.7 Motivation

Many authors have quantitatively studied the effect of dental implants and materials with a high atomic number on photon dose distributions. De Conto *et al.*, 2014, investigated the effect of dental restorations on 6 MV photon dose distribution with Monte Carlo simulation and experimental measurement. Measurements from three samples: a healthy tooth, a tooth with amalgam, and a crown in a simplified

configuration of H&N cancer treatment were assessed. Results indicated 23.8% backscattering dose enhancement for a tooth with amalgam. However, despite demonstrating attenuation, the consequences on the target volume were not reported [5]. Results like those presented by De Canto *et al.* were observed and supported by many other studies. Another study, Shimamoto *et al.*, 2015, investigated dose scattering due to nine dental metals in a single-field technique, three-dimensional conformal radiation therapy (3D CRT), and intensity-modulated radiation therapy (IMRT). They placed radiochromic films on dental metals in a water phantom and irradiated them with a 4 MV photon beam. For the single field method, compared to other dental metals, the gold metal had a measured scatter dose increase of 19.3% compared to the calculated scatter dose, while the dose scattering for 3D CRT and IMRT was less than that of the single field. [21].

Furthermore, Aziz and colleagues went a bit further from the study by De Canto *et al.*, 2014, to calculate the backscatter and attenuation effects of a healthy tooth, Amalgam, Ni-Cr alloy and Ceramco on normal tissue upstream and downstream of the incident 6MV and 15 MV photon beams, respectively. The results indicated that overriding CT numbers in regions corresponding to the high-density material with CT numbers that scale with the material's electron density can improve the accuracy of dosimetry calculations in the treatment planning systems (TPSs) [4].

Additionally, studies also showed that applying a metal artifact reduction (MAR) algorithm can minimize errors in dose calculation. In some cases, the focus

was placed on one algorithm while others compared two or more. In 2013, Spadae *et al.* considered the capacity to restore correct HU values by a MAR algorithm for titanium and Cerrobend within a phantom. The study used a Gammex phantom filled with different materials with a slot for inserts located in a defined PTV region. The phantom was scanned three times with three different inserts used: titanium, Cerrobend and solid water. The study showed that the error in dose calculation was up to 23.56% for the defined planning target volume (PTV) region when Cerrobend was present. However, the error was reduced to 0.11% after use of a MAR algorithm. In conclusion, the dose calculation was more accurate after the MAR algorithm improved image quality. Thus, retrieving correct HU values should be the primary evaluation criterion for a MAR algorithm [16].

In summary, many studies investigated the effect of metal artifacts on dose calculations [21] [22], while others compared the difference in dosimetry when metal artifact reduction algorithms and techniques were implemented [9] [11] [23]. Some cases also looked at the effect of overriding HU values on dose and methods to improve its effect on dosimetry calculations [17] [18] [13]. At the Juravinski cancer centre, the treatment planning protocol adapts some of the methods and findings found in studies. However, the impact of overriding the region of metal artifacts with density is not fully understood. It is well established that the treatment planning process is a complex procedure with the constant need for improvement. Therefore, this study would evaluate the current planning process using a holistic approach. To this effect, a head phantom containing dental implants at the level of

the oral cavity would be constructed and scanned using various protocols on two different commercial scanners to assess the appearance of artifacts. An MVCT image set would be merged with the kVCT image to improve visualization of the dental implants for use in density overrides. Single beam irradiations would then be performed in twelve geometries. The influence of density overrides values on agreement between calculation and measurement will be investigated for each geometry and imaging modality. Results would be compared to the current guidelines and suggestions made to both optimize the process and improve dose calculations.

CHAPTER 2

MATERIALS AND METHOD

2.0.1 Phantom

A selected region in a head and neck scan in the treatment planning system (TPS), Pinnacle³ (Figure 2.0.1), provided a template for a head phantom. Featured is an axial section at the oral cavity level, 5 cm in length in the superior/inferior direction. The phantom was divided into three regions of interest (ROIs); a block representing the mandible and teeth labelled as the dental tray (red outline), the front of the head (solid gray) and the back of the head (solid red) to accommodate printing. Furthermore, the dental trays were equipped with ionization chamber inserts, using a three-dimensional CAD program, Autodesk Inventor (San Rafael, California, 2020), within the oral cavity for measurement (Figure 2.0.2).

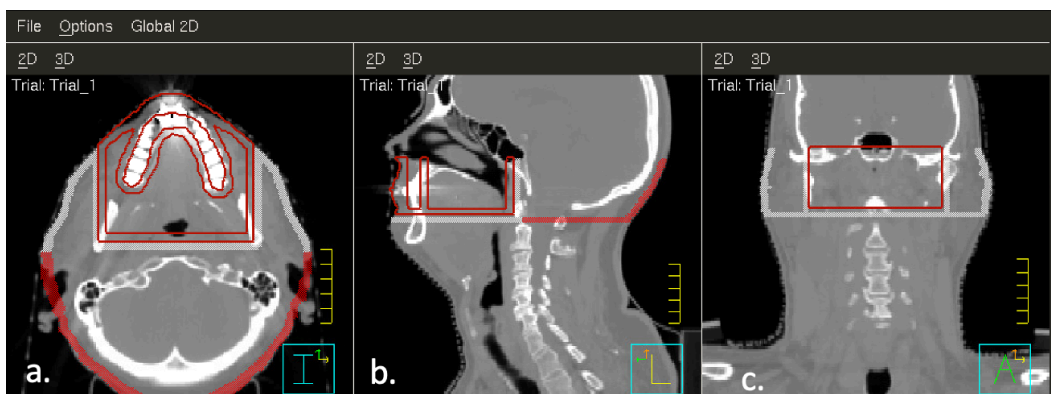


Figure 2.0.1: a) Axial, b) sagittal, and coronal CT scan of a head and neck patient.

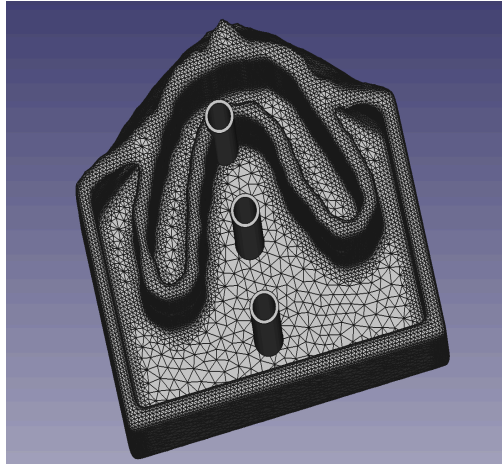


Figure 2.0.2: Illustration of dental tray in Autodesk Inventor equipped with ionization chamber inserts.

The head shell and three interchangeable dental insert trays were three-dimensional (3D)-printed with polylactic acid (PLA), using a 3D printer (Ultimaker 2+, Ultimaker B.V., Framingham, MA, USA). Next, the shell and trays were filled with regular modelling wax to mimic the attenuation of an average male head with a density of 0.92 g/cm^3 . Afterward, assorted dental work and restored human teeth were fixed into the simulated mandible (with a density range of $1.85\text{-}2.14 \text{ g/cm}^3$) comprised of lab plaster (density of 2.12 g/cm^2). For the tray labelled tray one, amalgam and Co-Cr-Mo alloy dental implants were imbedded into the tray. Tray two was configured with implants containing amalgam and gold that were set into the positions corresponding to tray one. (Figure 2.0.3a -2.0.3b). The dental work was then overlaid with more wax (Figure 2.0.3c). Dental work was only added to two trays (one and two), while tray three operated as a reference tray with the same materials used for walls and wax. All the trays were printed from the same

template. The samples were natural teeth repaired with amalgam and gold (tray two), and stainless steel or Co-Cr-Mo alloy and amalgam (tray one) implants from a nearby dentistry clinic. Definite compositions of the dental work received were unknown. Plugs made of the material, Nylon 6,6, with a diameter of 0.8 cm were also created for the ionization chamber inserts when not in use as its density is close to that of tissue. These plugs were left in the phantom and only removed if replaced by the ionization chamber. Finally, the head phantom was mounted onto a stand with the phantom representing a patient in the supine position (Figure 2.0.3b).

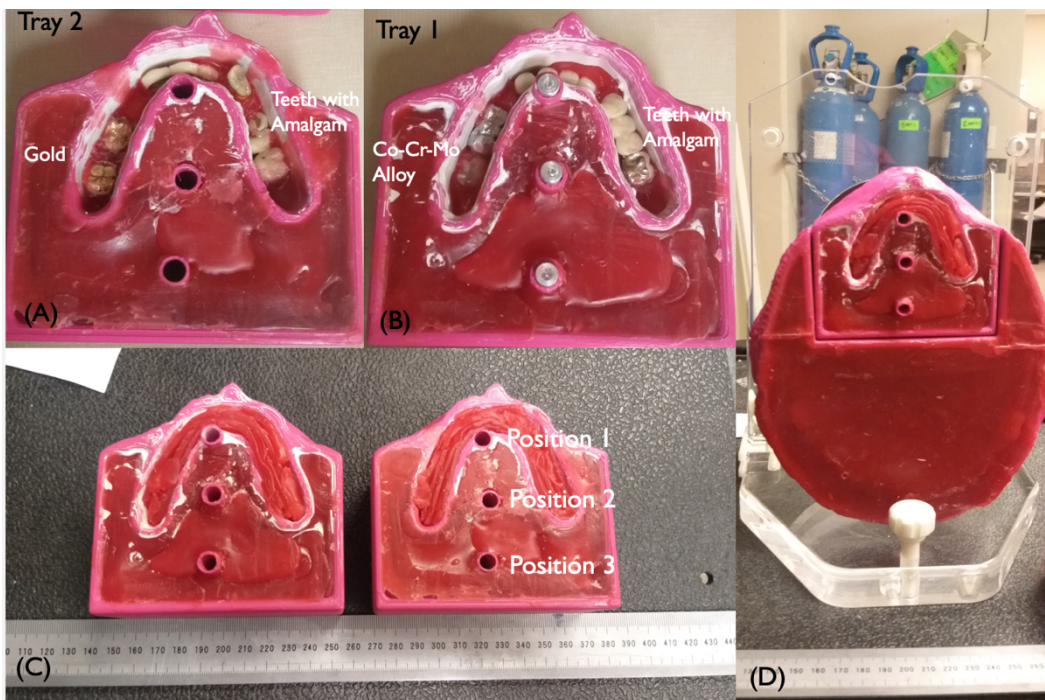


Figure 2.0.3: A) Interchangeable tray one and B) tray two, containing chamber inserts, dental implants, wax. C) Shows implants covered with wax with positions 1-3 indicated and the D) head phantom mounted on a stand.

2.0.2 Computed Tomography (CT) Imaging

For the acquisition of images, two CT scanners were used, Philips Brilliance Big Bore CT (Philips Healthcare, Amsterdam, the Netherlands) using peak energy 120 kVp, with and without the OMAR algorithm and Siemens SOMATOM® Definition AS (Siemens Healthineer, Erlangen, Germany) using peak energies 120 kVp and 140 kVp (DECT), with and without the iMAR algorithm. The Siemens SOMATOM Definition AS CT is a dual-source DECT with the capability to create monoenergetic images. To acquire a DECT image, scans at peak energies of 140 kVp and 80 kVp (80/Sn140 kVp) were taken. Unfortunately, the option to acquire a spectral combination of the two energies was not available at the time of this study. Therefore, only the 140 kVp images were used for their reduced susceptibility to beam hardening. For this study, the Philips machine was referred to as 'CT2' while the Siemens identified as 'CT3'.

Images were acquired with a field of view of 300 mm, a slice thickness of 2 mm and an increment of 2 mm. Helical CT protocols were used for both CT scanners. The images were reconstructed using filtered back projection (FBP), a standard (B) reconstruction kernel for CT2 and a H20f smooth (Vascular) reconstruction kernel was used for CT3. The choice of a softer reconstruction kernel for both CT scanners was based on the kernels commonly used in the cancer centre for CT examinations in the head area and based on the results from a study that assessed the effect of softer and sharper kernels on images and found that sharper kernels had less reduction in noise [9].

In addition to datasets with the metal hardware (Figure 2.0.4), an image dataset of the dental tray without metals was acquired to have an artifact-free image set available for contouring walls, wax, ionization chambers, and tissue.

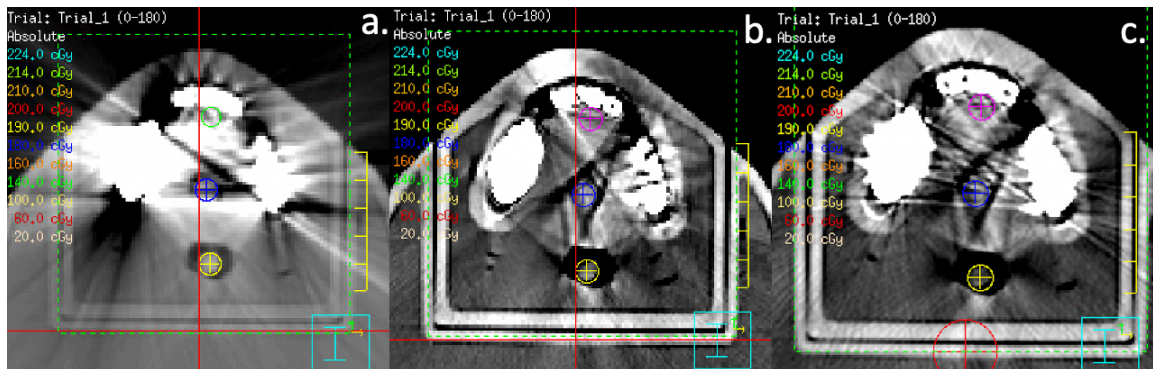


Figure 2.0.4: Same CT-slice with artifacts due to dental prostheses in tray one using a) CT2-OMAR, b) CT3-IMAR and c) CT3-140 KV.

2.0.3 MVCT Imaging

The phantom (trays one and two) also underwent imaging with an MVCT scanner, Varian Halcyon (Varian Medical Systems. Inc, Palo Alto, CA, USA). The Varian Halcyon includes an ultrafast 6 MV flattening filter-free (FFF) cone-beam computed tomography (MV-CBCT). CBCT is an alternative to the traditional computed tomography (CT) system. During a CBCT scan, the imaging machine rotates entirely around a patient's head using a cone-shaped x-ray beam. Many images are captured from various angles and rapidly reconstructed into three-dimensional (3D) images of the patient's anatomy [15]. MVCT scans were acquired at 6MV, with a field of view of 28 cm and a slice thickness of 2 mm. The MVCT images showed a considerable reduction in artifacts providing better visualization

of dental implants. Scans were transferred to the TPS, Pinnacle³, where they were fused with the corresponding kVCT image data to create hybrid image sets. The fused image consisted of both images aligned with each other to allow for regions of interest (ROIs) from the MVCBCT image to be properly transferred to the kVCT image used to override the density of implants (Figure 2.0.5).

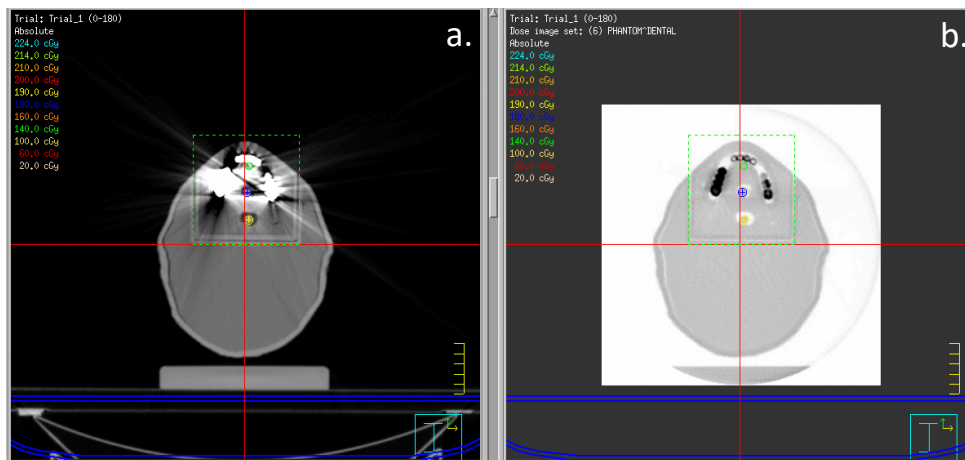


Figure 2.0.5: Comparison of dental artifacts in tray one between a) kVCT (grayscale) and b) MVCBCT (inverse grayscale) image sets.

2.0.4 Manual Artifact Correction

Efforts to reduce metal artifacts utilize three different approaches. The first and second methods are concerned with MAR algorithms and DECT, respectively. The third approach includes the manual correction of the artifacts using the contouring tools in Pinnacle³. In the relevant correction region, a region of interest (ROI) is defined, which encloses the artifacts. For streaking artifacts and dark bands, ROIs are defined by the contours created on the CT image of the dental reference tray with no artifacts. These contours outline the walls of the phantom made from PLA,

the areas filled with wax and plaster and the ionization chamber inserts filled with plugs made of nylon 6,6. The reference CT images and the CT image containing artifacts were merged, and the ROIs were exported to the images with dental work. The density of each ROI was replaced with the known density of the material (Table 2.0.1).

Material	Physical density (g/cm ³)
PLA Bolus	1
Regular Dental modelling wax	0.92
Lab Plaster	2.12
Nylon 6,6	1.14
Amalgam	8-9
Gold	19.2
Stainless Steel	8.1
Cr-Co-Mo	7.9

Table 2.0.1: Physical Density of the materials used in density overrides.

Regions of interest, ROIs were created on the MVCBCT images outlining the dental work, the MVCBCT and kVCT images were merged, and the ROIs were exported to the kVCT images. Within these ROIs, the CT number is at a threshold of 4096 for materials denser than bone. In this segmented area, the CT number is replaced with a density (density override) that best represents the material in the case of no artifact disturbance.

2.0.5 Treatment Planning

Five different kVCT scan modalities were used for both tray one and tray two: CT2 (O-MAR), CT2 (NO-OMAR), CT3 (IMAR), CT3 (NO-IMAR) and CT3-140 KV scans. Note that CT3- 140 KV is a MAR reconstructed image set. Contours were created in the region of interest section using the auto-contour tools that encircled regions containing a range of the CT number. Walls and wax were contoured individually from the CT scan of the phantom loaded with the tray containing only wax. Contours from the MVCBCT scans of tray one and tray two (dental implants) were created by contouring the saturated regions. Contours were used to precisely define the phantom geometry in the absence of artifacts (Figure 2.0.6). Points of interest (POIs) were created at the effective measuring volume of the AISL (Exradin AISLMR, 0.053 cm³, Standard Imaging. Inc, Wisconsin, USA) ionization chamber with a diameter of 0.8 cm positioned at the level of maximum artifacts (2 cm from the bottom of the tray) for trays one and two at the three ion chamber inserts. POIs were also created at 2.3 cm from the bottom of the tray for tray one at the same three ion chamber inserts to determine contrast in measurements taken at different distances in the inferior/superior direction. POIs were labelled numerically, starting with the insert at the front of the oral cavity, directly behind dental work (labelled POI_1) to the points toward the center of the head away from dental work (labelled POI_2 & POI_3) in a sequential manner (Figure 2.0.6b).

Two hundred monitor units (MU) were used for every single beam isocentric irradiation. Beams were delivered in twelve geometries: 0, 15, 45, 90,

135, 165, 180, 195, 225, 270, 315 and 345 degrees with the isocentre located at a depth of 5.2 cm within the dental tray at the level of major artifacts (5.2 cm in the anterior direction and 6 cm in the superior direction from the laser coordinates) for all angles except for the gantry at 0° and 180°. For the gantry at 0° and 180°, the isocentre was located at 10.4 cm within the dental tray at the level of major artifacts (6 cm in the superior direction from the laser coordinates) (Figure 2.0.6a-2.0.6b). The collimator had a rotation angle of 0° with a field size of 8 cm x 5 cm projected to the isocentre plane with the isocentre positioned at the respective depth for each beam within the dental tray from an axial view. Despite differing gantry angles, all beams were set up using the SAD technique (Source-Axis Distance of 100 cm) (Figure 2.0.7b). The dose was calculated for all three ionization chamber positions in each geometry. This was done for all image modalities. Calculated dose for images without contours (manually uncorrected), images with contours (manual overrides of walls and wax), and images with contours of walls, wax, and density overrides of dental implants were determined. Calculated dose distributions were then evaluated with respect to the measured dose.

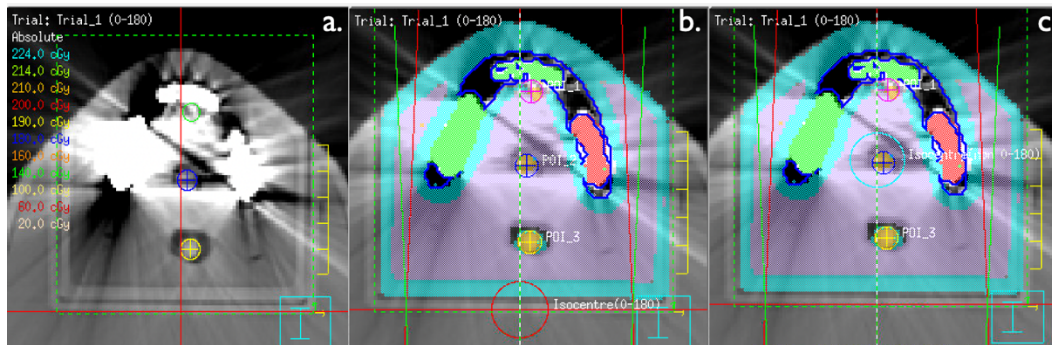


Figure 2.0.6: Comparison of a) uncorrected image and b) image with contours of walls, wax, and density overrides of dental overrides of implants. Image (b) also shows positions 1-3 and the isocentre (red circle) for the gantry at 0° and 180° outlined and labelled. Image c) shows the isocentre (blue outline) for the gantry angles excluding 0° and 180° .

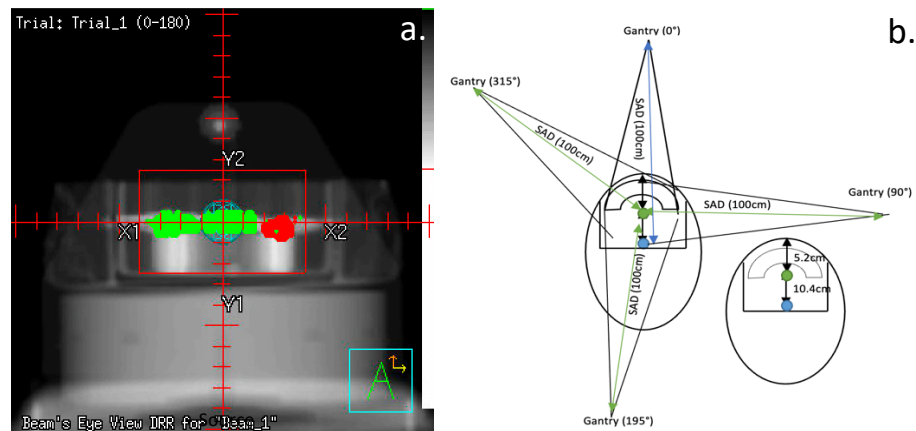


Figure 2.0.7: Illustrations showing a) the digitally reconstructed radiograph (DRR) of the phantom in a beam's eye view for gantry angle 0° . An isocenter is displayed as a sphere in blue, and dental implants are shown in red and green, respectively, b) irradiation geometry parameters linking the source and target (phantom) for gantry angles 0, 90, 195, 315.

CHAPTER 3

EXPERIMENTAL MEASUREMENTS

3.0.1 In-phantom Measurements

Dose was measured at three points in the phantom using an ionization chamber (Exradin AISLMR, 0.053 cm³, Standard Imaging, Inc, Wisconsin, USA) detector (4.0 mm in diameter and 1.1 mm thick) and corresponding calibrated electrometer. The unused ion chamber inserts were plugged while measurements were taken at each position as shown in Figure 3.0.1a. The AISL ion chamber is designed to measure absolute dose (within an area of 1cm²) to water using the TG-51 protocols [24]. The inserts created in the phantom permitted the positioning of the detector perpendicular to the beam direction at positions 1-3 (Figure 3.0.1).

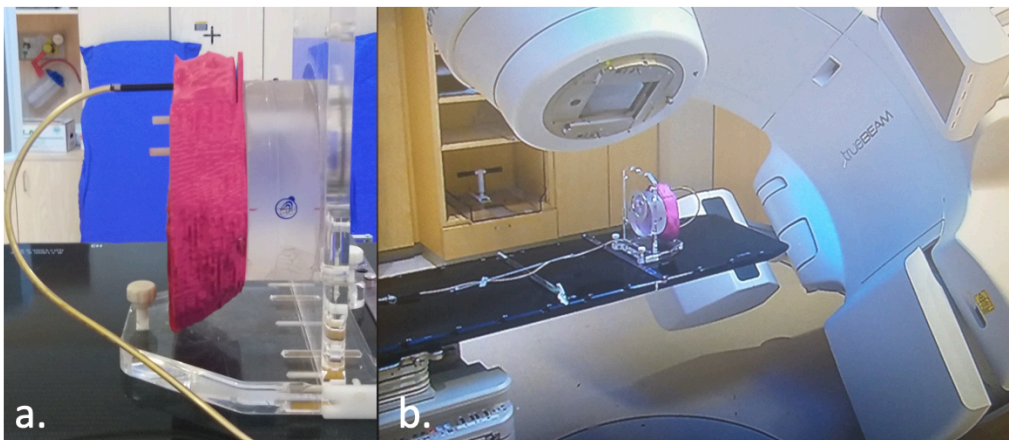


Figure 3.0.1: Phantom set up on the treatment couch with the a) ion chamber in position 1 with the cable leading to the electrometer outside the treatment room and the b) phantom undergoing irradiation at a gantry angle of 315 degrees.

A setup laser alignment system was used to position the head reproducibly. Anterior and lateral reference marks on the phantom were aligned with three setup lasers. Couch shifts were then applied to position the isocenter according to the required treatment geometry. The isocenter was positioned as planned, as described in section 2.0.5. These shifts required no left/right couch adjustments, a move of 5.2 cm down and 6.0 cm out (away from the gantry) for all angles except for the gantry at 0° and 180°. For the gantry at 0° and 180° the couch only moved 6.0 cm out. The setup allowed the couch to remain at an angle of 0° throughout treatment with only the mentioned shifts in the anterior and superior directions (Figure 3.0.2a-3.0.2b). The TrueBeam Linear Accelerator (Varian Medical Systems. Inc, Palo Alto, California, USA) was programmed to deliver 200 MU to the phantom with a static 6 MV photon beam.

Accumulated charge was measured with the AISL/electrometer pair for each irradiation of 200 MU from the TrueBeam unit. This process was performed for all twelve (12) gantry angles at positions 1-3 for trays one and two at 2 cm from the base of the tray (the detector located at the center of artifacts) and tray one at 2.3 cm from the base (the detector located at the edge of artifact field). The absolute dose was calculated and compared to the dose calculated in the TPS, Pinnacle³. Measurements were taken at two distances from the base of the tray for tray one at the three positions to observe the effect on agreement between calculated dose and measured dose as the distance from artifacts increased in the anterior/superior direction.

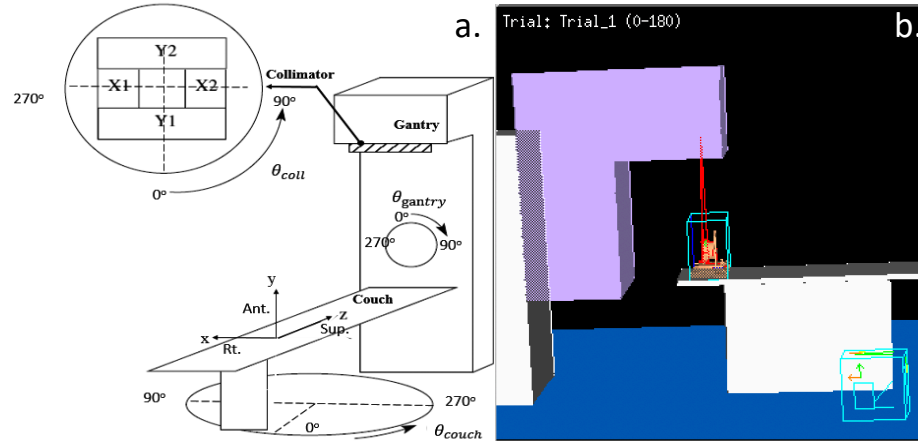


Figure 3.0.2: a) Illustration showing irradiation parameters from a view of the treatment room and a b) three-dimensional room's eye view of the set up for the gantry at 0° , in the TPS.

3.0.2 Measured Absolute Dose

Accumulated charge (nC) was recorded from the calibrated electrometer. To determine the absolute dose, the AAPM's TG-51 protocol for clinical reference dosimetry was used [24]. In addition to charge (nC), the temperature and pressure at the time of treatment were also recorded. Values were entered into the following equation:

$$M = P_{ion} P_{TP} P_{elec} P_{pol} M_{raw} \text{ (nC)} \quad (\text{Eq 3.1})$$

M_{raw} is the uncorrected ion chamber reading at the point of measurement for a given number of monitor units (nC). M is the ion chamber reading adjusted to the standard environmental conditions of temperature and pressure corrected for polarity effects and ion collection efficiency. The calibration factor, P_{TP} , is given for standard

environmental conditions of temperature at 22 °C and pressure at one atmosphere (101.33 kPa). The temperature (T) and pressure (P) at the time of measurement were recorded and the calibration factor determined [24].

$$P_{TP} = \frac{273.2 + T}{273.3 + 22.0} \times \frac{101.33}{P} \quad (\text{Eq 3.2})$$

Furthermore, P_{elec} , the electrometer correction factor, was assigned a value of 1.00 as the electrometer and ion chamber were calibrated as a pair. P_{ion} was previously measured to be 1.001 for a 6 MV beam produced by the TrueBeam machine used in this study. P_{ion} rectifies incomplete ion collection efficiency in the measurement. P_{pol} was also previously measured to correct for polarity effects and found to be 1.001.

The absolute dose to water/tissue in cGy at the point of measurement of the ion chamber was determined from the corrected ion chamber reading, M, using the equation:

$$M \frac{Q}{W} = M k_Q N_{D,w}^{60Co} \quad (\text{cGy}) \quad (\text{Eq 3.3})$$

$N_{D,w}^{60Co}$ (cGy/nC), known as the Cobalt 60 calibration coefficient, is the absorbed dose to water calibration factor for an ion chamber located in a Co^{60} beam [24]. For the ion chamber and corresponding electrometer combination used in this study, the coefficient is $56 \pm 1\%$ s.dev.cGy/nC. The quality conversion factor, k_Q , is used to

transform the Co⁶⁰ calibration factor to the corresponding factor in any beam quality Q for photons. The quality conversion factor for the A1SL ion chamber in a 6 MV photon beam was previously measured to be 0.993 for the treatment machine used.

Absolute dose (cGy) was then calculated, and the measured dose was compared to the calculated dose in the TPS, Pinnacle³ for all conditions.

3.0.3 Percent Dose Error

The percent difference between the calculated and absolute measured doses was determined as a method of comparison using the equation:

$$\text{Percent Error} = \frac{Dose_{\text{calculated}} - Dose_{\text{measured}}}{Dose_{\text{measured}}} \times 100 \quad (\text{cGy or Gy}) \quad (\text{Eq. 3.4})$$

Percent Error was calculated for each calculation scenario: images without contours (manually uncorrected), images utilizing CT # to density table for a head geometry, listed in the physics section in the treatment planning system as opposed to the table used clinically; images with contours (manual overrides of walls and wax); and images with contours of walls, wax, and density overrides of dental implants. The percent error was determined at detector positions 1, 2 and 3 for tray one and tray two with the effective point of measurement 2 cm from the base of the tray (corresponding to the center of the artifact field) and tray one with the effective point of measurement 2.3cm from the base (corresponding to the edge of the artifact

field). Table 3.0.1 shows the percent error for tray two, with manually uncorrected images at gantry angle zero. A total of thirty-six such tables were generated corresponding to 12 gantry angles. For tray one and tray two at 2 cm with the effective point of measurement at 2 cm from the base of the tray (the detector located at the center of artifacts), twenty-four tables were produced (Figure 3.0.3a-3.0.3b). Figure 3.0.3a shows tray one with the effective point of measurement at 2.3 cm from the base of the tray produced another twelve tables for each angle from the base (the detector located at the edge of artifact field).

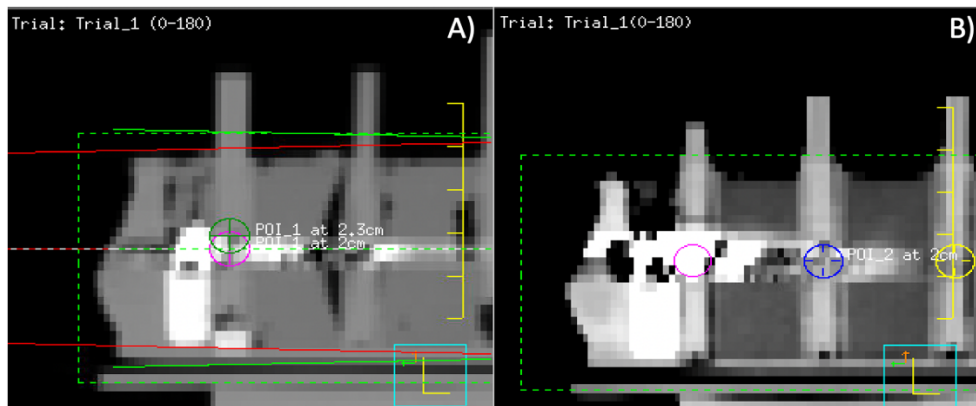


Figure 3.0.3: Sagittal CT image of A) tray one showing the effective point of measurement at 2 cm (purple) and 2.3 cm (green) for POI_1 and of B) tray two with the effective point of measurement at 2 cm (purple).

Position	Measured (cGy)	Percent Error %				
		CT2-No OMAR	CT2- OMAR	CT3-No IMAR	CT3- IMAR	CT3- 140kVp
1	205.5	1.9	7.4	1.8	7.1	5.9
2	184.4	-0.74	3.2	-0.2	5.2	3.9
3	155.5	-0.3	3.9	-0.5	6.6	5.1

Table 3.0.1: Percent dose error (%) for the various modalities of tray two consisting of teeth with amalgam and gold implants. The CT image was manually uncorrected. The phantom was irradiated with a 6 MV photon beam for the gantry at 0°.

CHAPTER 4

RESULTS AND DISCUSSION

4.0.1 Initial Results

Figures 4.0.1(a)–4.0.1(e) show CT images of the same representative slice with artifacts before metal artifact reduction (MAR) techniques and after application of MAR reconstruction. Compared to the OMAR reconstruction (Figure 4.0.1a), the IMAR reconstructed images both at 120 kVp (Figure 4.0.1b), and 140 kVp (Figure 4.0.1c) show fewer streak artifacts, however IMAR at 140 kVp has a larger saturation region than the 120 kVp which is contrary to expected. Meanwhile, the images without IMAR reconstruction (Figure 4.0.1e) show the most streak artifacts.

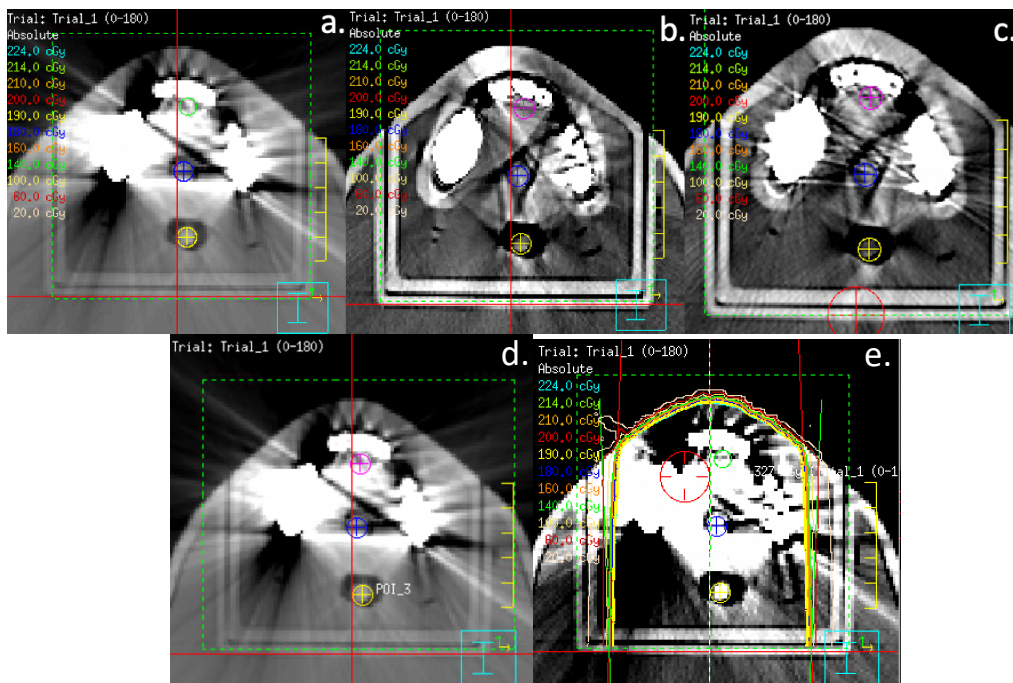


Figure 4.0.1: Same CT-slice with artifacts for tray one categorized by MAR reconstructed images a) CT2-OMAR, b) CT3-IMAR, c) CT3-140 KV IMAR, and the uncorrected images d) CT2- NO OMAR and e) CT3- NO IMAR data sets.

Percent error calculations were used to demonstrate the influence of artifacts and saturation of pixels in regions of high-density from Figure 4.0.1. The percent error is expected to establish that the artifact-afflicted image data creates a characteristic dose deviation between the calculated and measured doses. When the percent error is positive, the calculated dose is greater than the measured dose, which indicates that the beam is incident a region of higher density than that modelled in the CT dataset. Additionally, a modelled beam may pass through a region containing saturated pixels to further enhance the effect of saturated pixels or dark streaks on calculated dose. Dark streaks obscure denser implants with regions of lower density while saturated pixels limit density representation to 2.866 g/cm^3 or a CT number of 4095. Figures 4.0.2 (A) & (B) demonstrate the correlation between CT number and dose (cGy) with given depth resulting in a positive percent error. The calculated dose (blue) is greater than the measured dose (red) because the clipped CT number in the sample region reflects a lower density than the implant.

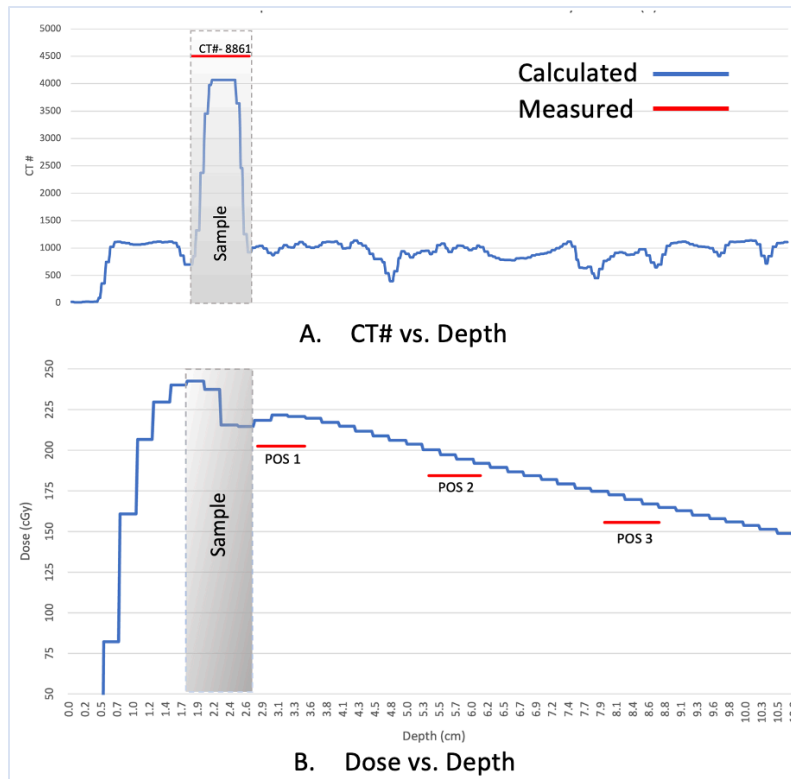


Figure 4.0.2: Data collected from the CT2-OMAR, tray two reconstruction image set, at a gantry angle of 0^0 using the CT to Density Table 'JCC_Avg_Mar_09'. Graphs show A) Comparison between the TPS's clipped CT number and the extrapolated CT number corresponding to a known density of 8g/cm^3 for amalgam, labelled in red and B) Calculated dose and measured dose at detector positions 1-3. Error bars for measured dose are smaller than symbol size.

When the percent error is negative, the measured dose is greater than the calculated dose, indicating the modelled beam is passing through regions containing bright (high CT number) streak artifacts. Figures 4.0.3 (A) & (B) demonstrate the correlation between CT number and dose (cGy) with depth resulting in a negative percent error. The measured dose (red) is greater than the calculated dose (blue) due to excessive attenuation of the modelled beam. Figure 4.0.3A also corroborates that the clipped CT pixels represent a larger area than the actual implants.

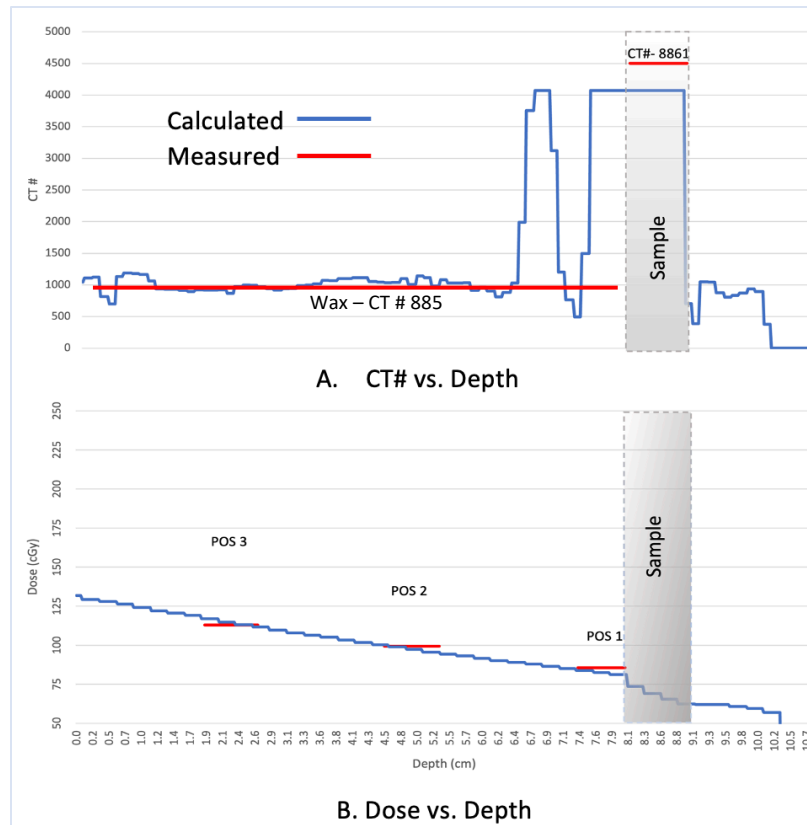


Figure 4.0.3: Data collected from the CT2 -OMAR, tray two reconstruction image set, at gantry angle 180° using the CT to Density Table 'JCC_Avg_Mar_09'. Graphs show A) Comparison between the TPS's CT number and the actual CT number of the sample (known density of 8 g/cm^3) and wax (known density of 0.92 g/cm^3) and the B) calculated dose and measured dose at detector positions 1-3. Error bars for measured dose are smaller than symbol size.

The two trays were irradiated using various gantry angles, for each irradiation, percent error was charted, and the trends were noted. Figures 4.0.4(A)-4.0.4(C) demonstrate the direction of the beam and the distribution of dose with respect to the three detector positions for tray one (Figure 4.0.4A) and tray two (Figure 4.0.4B) at 2 cm. The percent error for five imaging modalities is displayed for both trays at gantry angle 0° (Figures 4.0.4D & 4.0.4E). For gantry angle zero, the beam only passes through Amalgam.

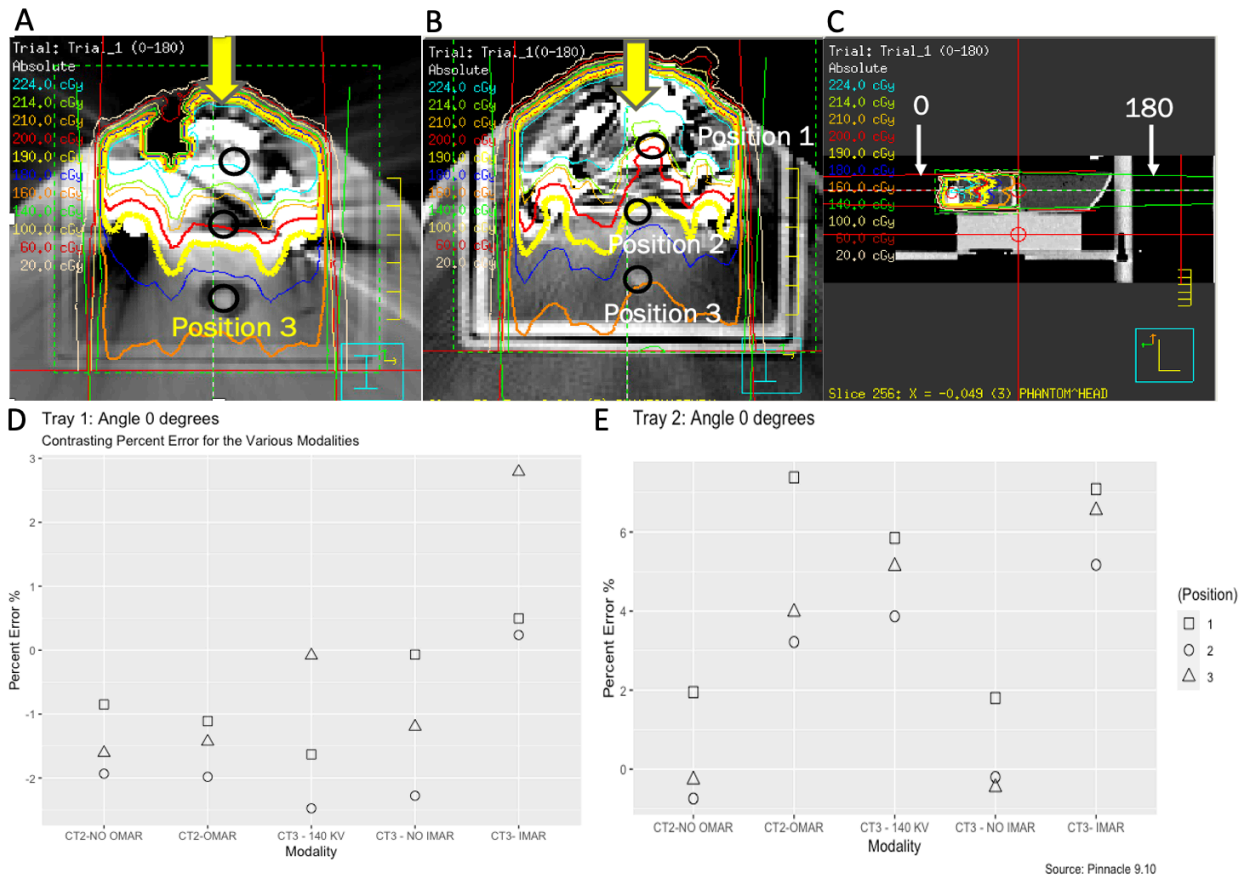


Figure 4.0.4: Comparison of percent error for various modalities and contrast of the data between trays one and two at the axial CT slice shown for the gantry at 0° . Tray one contains amalgam and an assumed Co-Cr-Mo alloy, while tray two has amalgam and gold materials. The axial OMAR reconstructed CT image with overlaid isodose lines is shown for tray one (A) and tray two (B) tray two illustrates the distribution of the absolute dose to the three detector positions using coloured isodose lines. (C) The beam angles are shown, with zero degrees (red lines) entering the mouth. Contrast of the various modalities were performed for tray one (D) and tray two (E) with the detector positions labelled by shape. Note that CT3-140 KV is a MAR reconstructed image set.

The 6MV photon beam passes through Amalgam before reaching detector position 1 for the gantry at 0° . As previously mentioned, it is predicted that the percent error will be positive as the modelled beam delivers a greater dose than in the physical treatment of the phantom. In Figure 4.0.4D, a positive percent error is seen with all

positions in the CT3-IMAR image data set, with the most prominent positive error at approximately 3%. However, data from the other imaging modalities result in a percent error that is negative, suggesting that saturation of CT number in pixels is offset by an increased area of saturated pixels. Bright streak artifacts then result in a calculation that is too low compared to measurement. The positive percent errors corresponding to CT3- IMAR were then further explored by comparing the CT number as a function of depth between the iMAR corrected image, CT3- IMAR and the uncorrected image, CT3- NO IMAR (Figure 4.0.5). The graph shows that the CT number before position one for CT3- NO IMAR (orange) data is twice as large as CT3-IMAR (black) at a depth of approximately 0.8 cm. This implies a more considerable reduction in dose for the uncorrected data set when compared to CT3-IMAR that increases with depth of measurement. Streak artifacts are represented by the subsequent peaks in the CT3- NO IMAR trace. These result in a radiological depth that is too large and corresponding calculated dose that is too low compared to measurement. In contrast, the IMAR corrected image yields a CT number trace that is relatively flat after the saturation region.

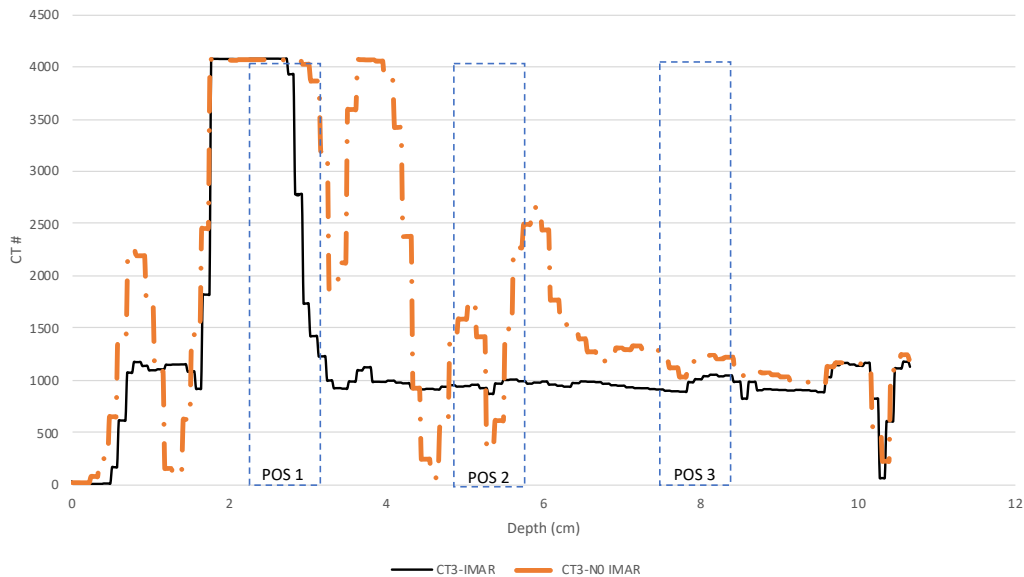


Figure 4.0.5: CT number as a function of depth in the TPS for the two image sets, CT3-IMAR and CT3-NO IMAR, for tray one for the gantry at 0° . Depth is measured in the direction of the beam angle (front of the mouth to the center of the head). Positions 1-3 are labelled.

In Figure 4.0.4E, a positive percent error is seen with nearly all positions in the various image data sets, position 1 having the largest positive error for all modalities. Results are as expected and reflect the influence of clipped CT pixels, which do not sufficiently attenuate the modelled beam as it passes through the implants causing the calculated dose to be higher than the measured dose. The graph also shows the influence of streaking artifacts beyond the saturated region as they tend to compensate for the clipped CT numbers by adding bands of elevated CT number. Thus, the percent errors at positions 2 and 3 tend to be smaller in magnitude than those at position 1. Figure 4.0.6 demonstrates the effect of the two phenomena by comparing CT2 – OMAR data for trays one and two. Tray one shows significant fluctuations in CT # when compared to tray two. This further suggests that for tray

one, the clipped CT number are sufficiently compensated by streaking artifacts to appropriately attenuate the beam. In contrast, the results for tray two are mostly influenced by the clipped CT numbers at the implant. Similar results were observed for the gantry at 15° and 195° for both trays.

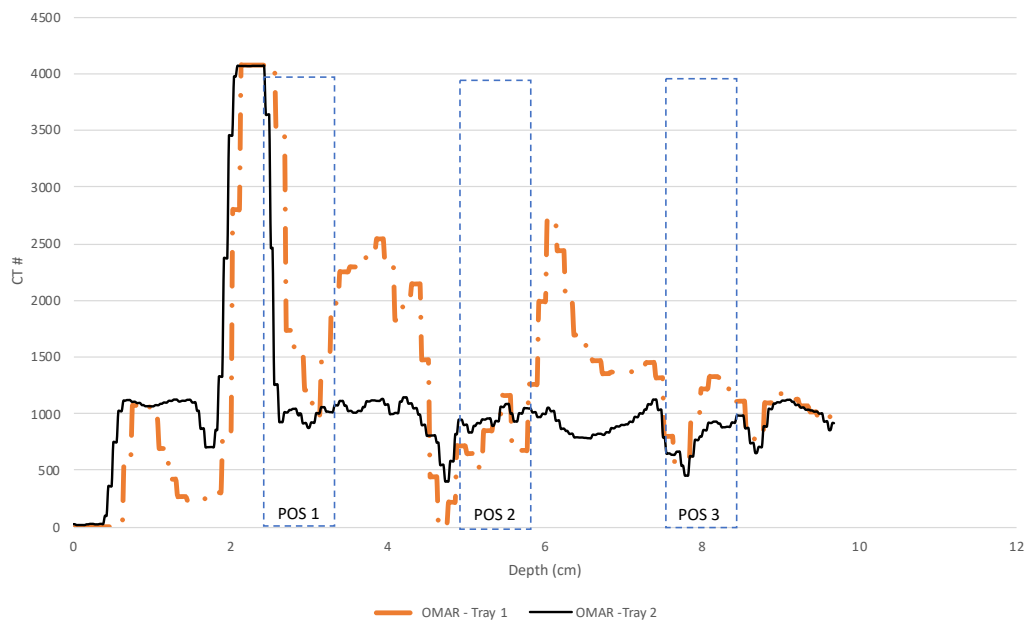


Figure 4.0.6: CT number as a function of depth in the TPS for the two image sets, CT2-OMAR, trays one and two at an angle of 0°. Depth is measured in the direction of the beam angle (front of the mouth to the center of the head). Positions 1-3 are labelled.

Data were further inspected for all other angles, and the results were grouped by the beam incident through Gold (head on and at an angle) and no implants. Recall that the information for the beam passing through dental Amalgam was already analyzed in Figure 4.0.4E. Tray two consisted of two materials, Amalgam and Gold. Figure 4.0.7 gives a summary of the trends observed and their implications.

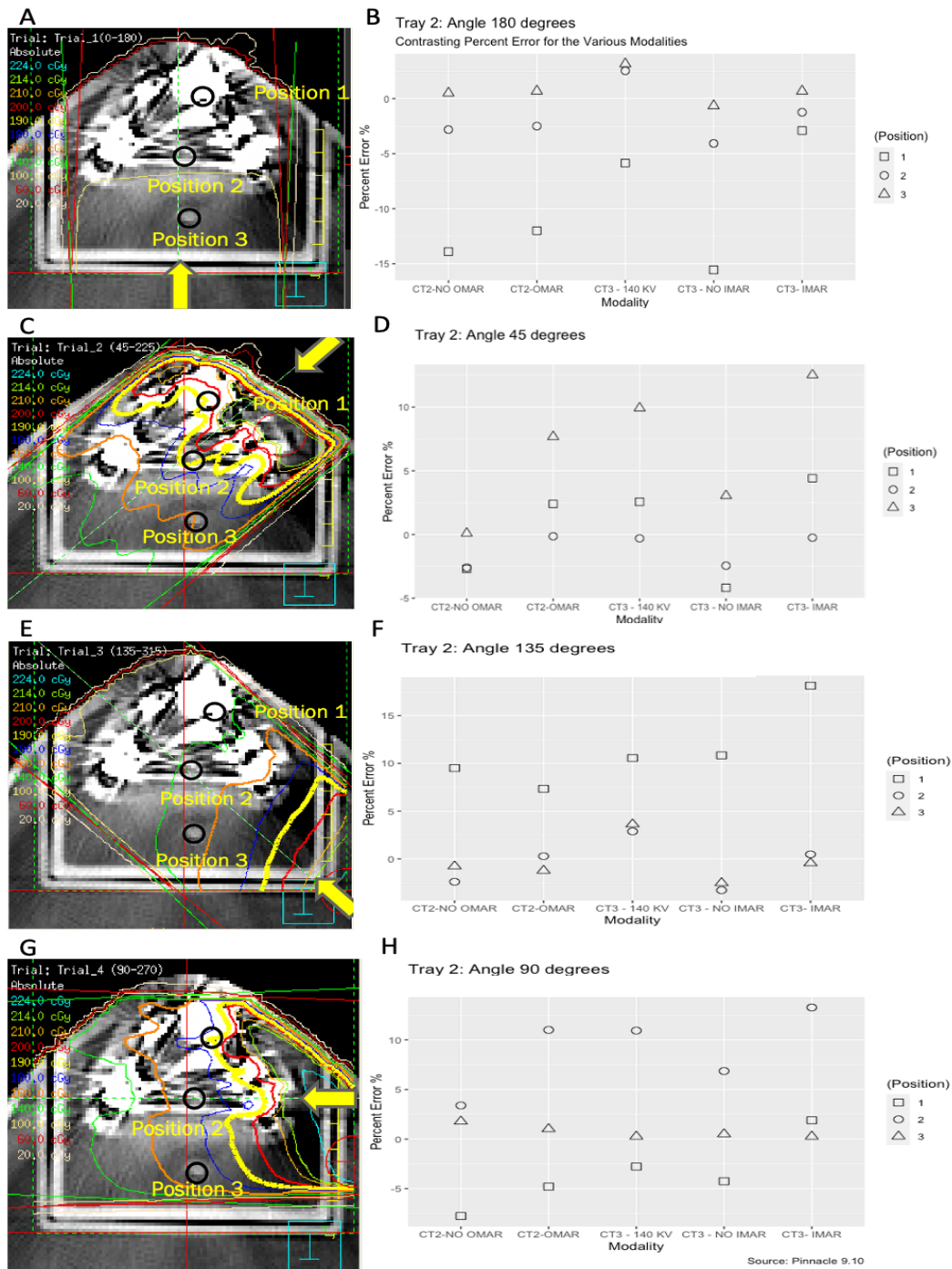


Figure 4.0.7: The images in the left column are Axial OMAR reconstructed CT images for tray one at various gantry angles with detector positions shown and coloured absolute isodose lines overlaid. The plots in the right column are the corresponding percent error by imaging modality for tray two consisting of Amalgam and Gold at various gantry angles. Shapes indicate positions 1-3. Note that readings were taken at 2cm from the base of the phantom in the region

consisting of significant artifacts. (A & B) Gantry at 180°; (C & D) gantry at 45°; (E & F) gantry at 135°; (G & H) gantry at 90°. Note that CT3- 140 KV is a MAR reconstructed image set.

With the gantry at 180°, position 1 (squares) yielded a significant negative percent error with a maximum of more than 15 % for CT3-NO IMAR (Figure 4.0.7A). This result was expected because streaking artifacts have a dominant influence since the beam does not pass through dental work. Additionally, the beam travels through most of the artifacts before arriving at position 1, which accounts for the significant disparity between the measured and calculated doses. The same is seen for position 2 (circles) but to a lesser extent as the beam does not pass through maximum streaking artifacts. For position 3 (triangles), the percent error tended to the positive axis due to slight cupping artifacts. Errors for position 3 were relatively small. Similar results were seen for angles 165 and 195.

With the gantry at 45°, the beam passes through regions of Amalgam and Gold before reaching positions 1 and 3. For position 1, the percent error tended to the positive axis for MAR corrected image sets. For uncorrected images, the percent error was slightly negative; this is due to clipped CT numbers for amalgam and streaking artifacts influencing the data, respectively. Figure 4.0.8 shows the contrast between CT numbers for CT3 -IMAR and CT3-NO IMAR. The graph reveals that the uncorrected CT3 image dataset had a higher CT number along the path to position 1 resulting in a smaller calculated dose when compared to the MAR corrected CT3 image. For position 2, the percent error was consistently small. The presence of gold in the beam path toward position 3 resulted in high positive percent

errors due to reduced attenuation from regions with clipped CT numbers in the TPS.

Similar results were seen for angle 315.

With the gantry at 135° (Figure 4.0.7F), the beam passes through Gold before arriving at position 1, resulting in high positive percent errors for the reason stated above. For positions 2 and 3, the percent error was reduced due to the presence of only minor streaking or cupping artifacts. Similar results were seen for angle 225. With the gantry at 90° (Figure 4.0.7H), the beam was directly incident on gold implants. Position 2, in this case, was most affected by the characteristic positive percent error due to clipped CT numbers. For position 1, the presence of streak artifacts consistently resulted in a negative percent error. For position 3, errors were small due to the presence of a small region of saturated pixels. Similar results were seen with the gantry at 270° .

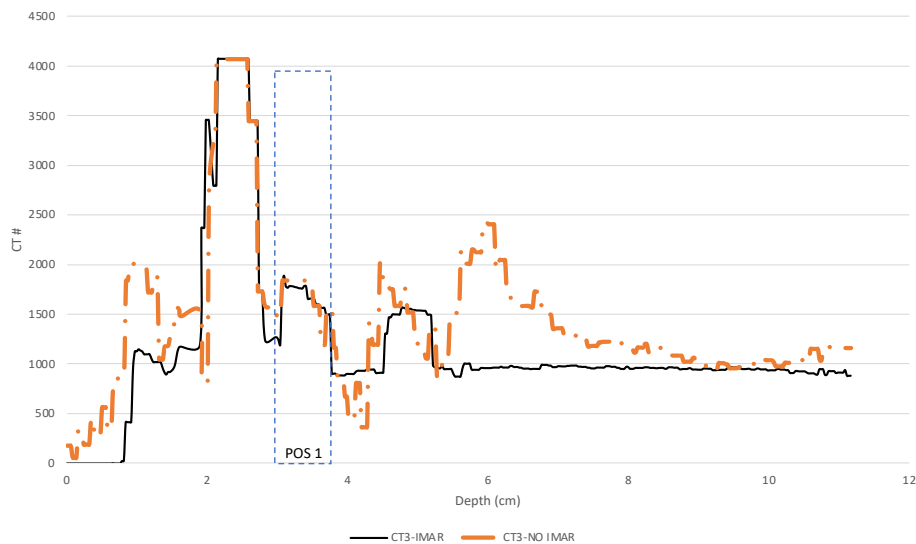


Figure 4.0.8: CT number as a function of depth in the TPS for the two image sets, CT3-IMAR and CT3-NO IMAR, for tray two at an angle of 45° . Depth is measured in the direction of the beam angle. Position 1 is labelled.

The error distribution was then categorized by position for trays one and two at all angles (Figure 4.0.9). Percent error at position 1 showed the largest spread due to the proximity of dental work and the subsequent artifacts. Percent error at positions 2 and 3 were progressively more clustered around 0% as distance from the implants increased.

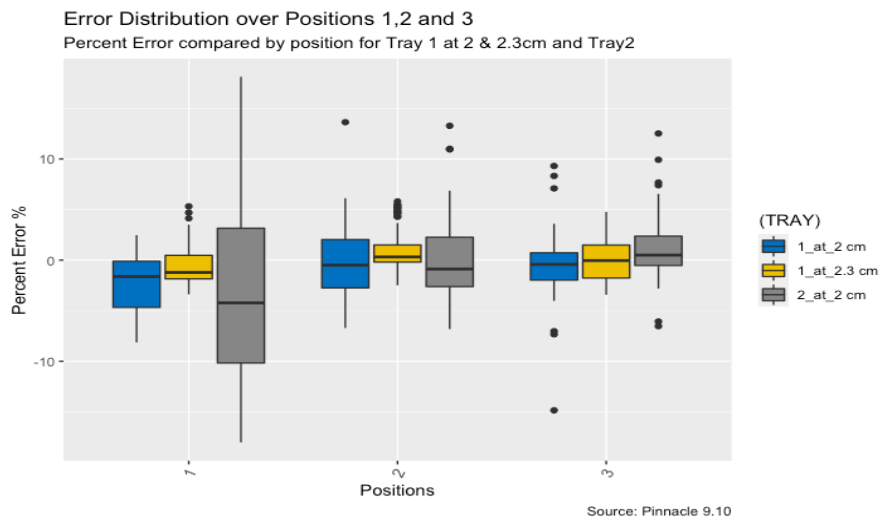


Figure 4.0.9: Distribution of Percent Error as a function of detector position for trays one and two, presented over all modalities and angles. Note that CT3- 140 KV is a MAR reconstructed image set.

Figure 4.0.10 shows the distribution of percent error by imaging modality and tray for all angles and positions. Note that tray one at 2.3 cm had similar medians of approximately 0 % with narrow distributions in all modalities except for CT3-140 KV. The large positive spread in percent error for 140 KV for all trays can be attributed to a large reduction in streaking artifact compared to CT 2 image sets seen in Figure 4.0.1a and Figure 4.0.1c. Additionally, Figure 4.0.1 shows an increase in the area containing saturated pixels for CT3-140 KV (Figure 4.0.1c) compared to CT 3-IMAR (Figure 4.0.1b) which can also be attributed to a more

positive percent error. Moreover, it was noted that tray one at 2 cm data had a negative skew of percent errors for all modalities characteristic of streaking artifacts. Meanwhile, tray two had a noticeable positive skew of errors attributed to the influence of clipped CT numbers in the region of cupping artifacts. Despite individual tray analysis, it was impossible to state which single modality had the best ability to reduce image artifacts resulting in a more accurate calculated dose in the TPS. This effect would be represented by the smallest range of percent error and a consistent median of approximately zero. However, it was noted that all trays for CT3-IMAR had a median percent error closest to zero (<1%) while CT2-OMAR appeared to have the tightest inter-quartile range (< +/- 2.5% error).

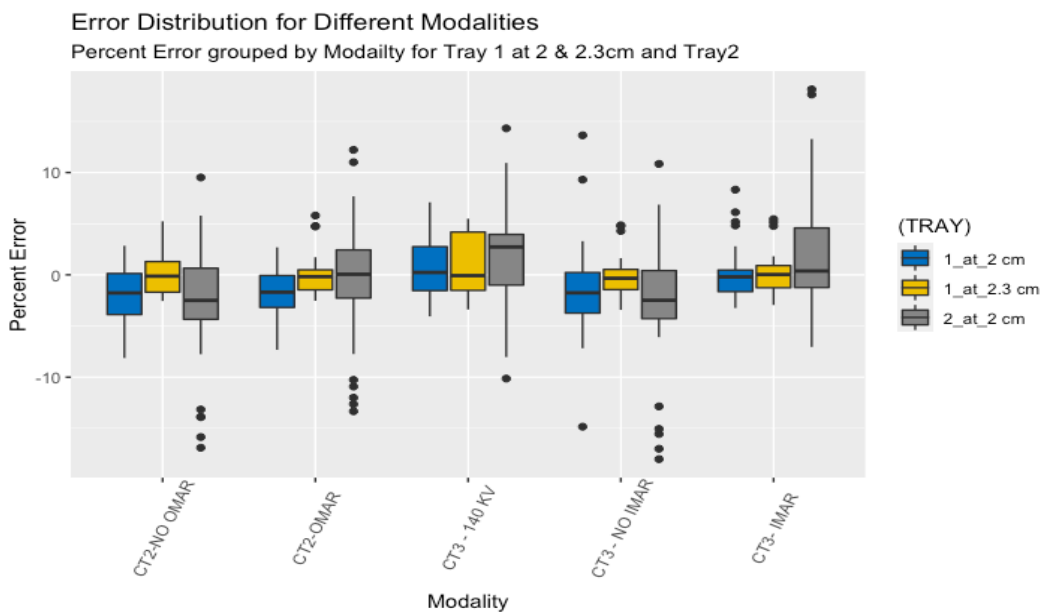


Figure 4.0.10: Distribution of Percent Error over all positions and angles related to modality for trays, one and two. For tray one, measurements were taken at 2cm and 2.3cm from the base of the phantom.

4.0.2 CT to Density Table

CT to Density tables within the TPS allow for the conversion from CT number to the density of the imaged material for the calculation of dose. The table is influenced by physical parameters such as x-ray energy; 140 versus 120 kVp; the commercial brand of CT machines; CT2 (Philips) versus CT3 (Siemens); the type of reconstruction algorithm; OMAR (CT2) versus IMAR (CT3); and the geometry of the density calibration phantom; head versus body. The various tables are plotted in Figure 4.0.11.

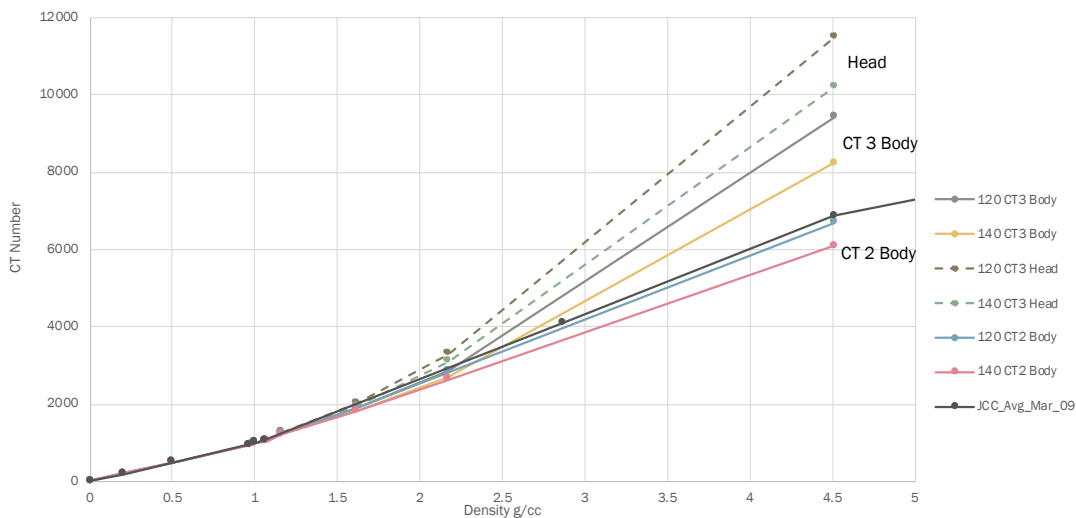


Figure 4.0.11: CT # to Density plots available for use within the TPS. The Reference table, 'JCC_Avg_Mar_09', is used clinically for all planned patients (Juravinski Cancer Centre, 2021).

The graph illustrates the difference in CT number for the same density value for independent CT scanners and phantoms. CT numbers beyond 4096 are extrapolated from data below this saturation limit for JCC_Avg_Mar_09 table. For the other tables, data at 4.5 g/cm³ are CT numbers from the calibration of a titanium

plug. Curves corresponding to the head geometry have a steeper slope than those corresponding to the body geometry. Similarly, curves corresponding to 120 kV photon energy have a somewhat steeper slope than those corresponding to 140 kV photon energy. Finally, curves corresponding to CT3 have a steeper slope than those corresponding to CT2. Since calculations presented above were based on the reference table, 'JCC_Avg_Mar_09', the work presented below in Figure 4.0.12 evaluates the effect of using alternative tables on the calculated percent errors.

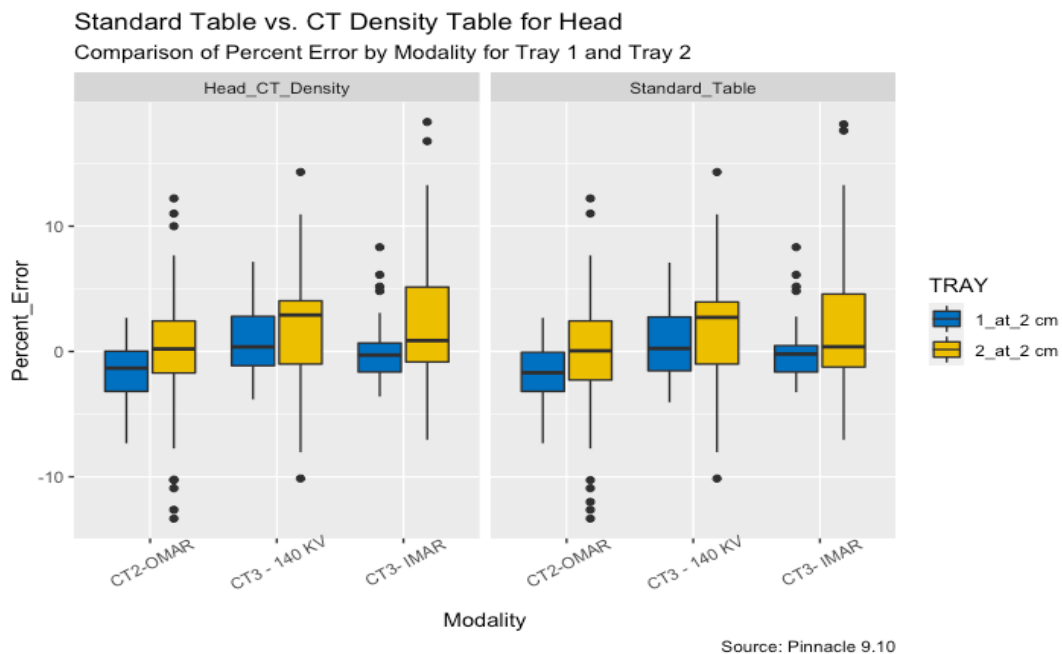
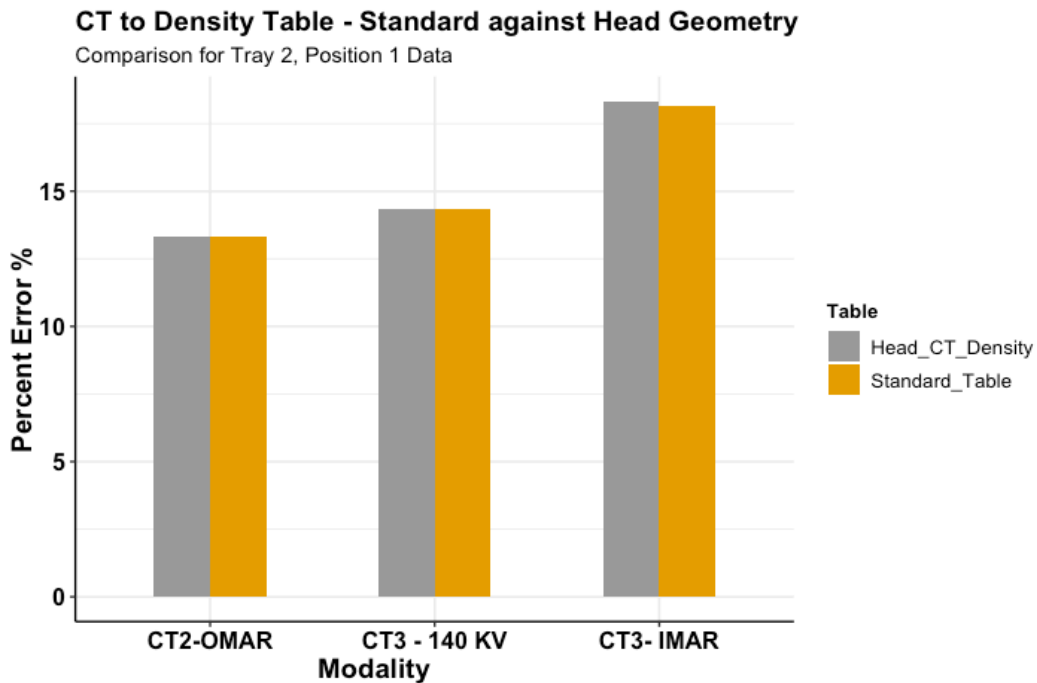


Figure 4.0.12: Distribution of percent error for all positions and angles related to modality for trays, one and two. The right plot represents calculations taken using the CT to Density table 'JCC_Avg_Mar_09'. The left plot represents calculations using the CT to Density tables measured using the head geometry.

The boxplots compare the percent error between "Head_CT_Density" for the different modalities and the reference table, JCC_Avg_Mar_09. The differences in distribution of percent error in the clustered data are insignificant. Further analysis

was done for a specific detector position and tray. Results are shown in Figure 4.0.13. The Bar graph shows no clear change in error across the modalities. It was therefore determined that the reference table is suitable for use in the remainder of this study.



Source: Pinnacle 9.10

Figure 4.0.13: Comparison of percent error between the Reference CT to Density Table and CT to Density (Head geometry) for position one of tray two, for all angles.

4.0.3 Contours (Walls and Wax)

Figures 4.0.14(A)–4.0.14(B) show CT images of the same representative slice with artifacts after application of MAR reconstruction and the addition of manual density overrides of walls and wax for only the MAR reconstructed image datasets. Percent

error was calculated after overrides were applied, and the change in the distribution was observed compared to the original data.

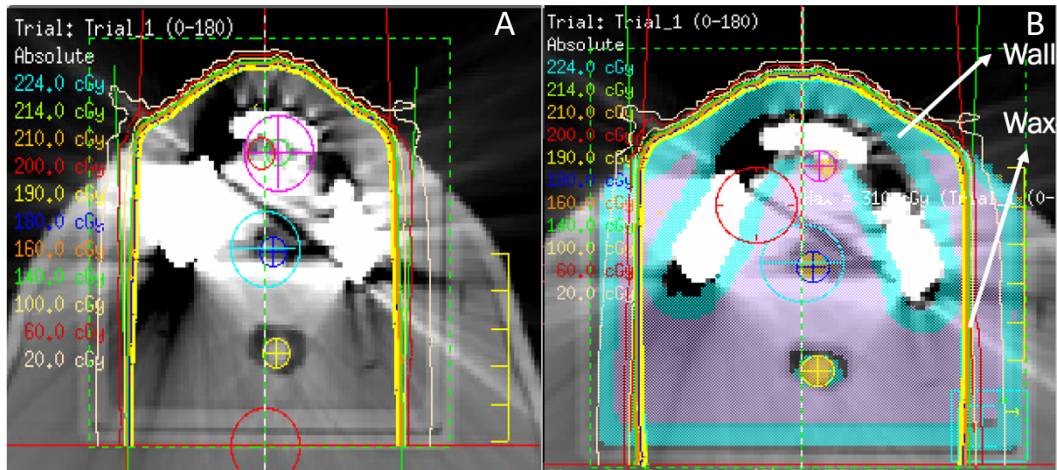


Figure 4.0.14: Image of the axial OMAR reconstructed CT image for tray one. The image on the left has (A) has no density overrides, whereas the image on the right (B) has manual density overrides corresponding to the walls and wax.

When density overrides were applied to the walls and wax, the effect of streak and cupping artifacts are negated. Since clipped CT pixels dominate in Figure 4.0.15, the override results in an overall higher calculated dose in the clustered data (recall that saturated regions have been shown earlier to increase the radiological path length). It is interesting to note that the range of data for tray one is reduced while that of tray two is increased when the density overrides are applied. This difference is attributed to the influence of saturated pixels in tray one compared to tray two which contains Gold. Figure 4.0.16 further demonstrates these findings for two measurement geometries.

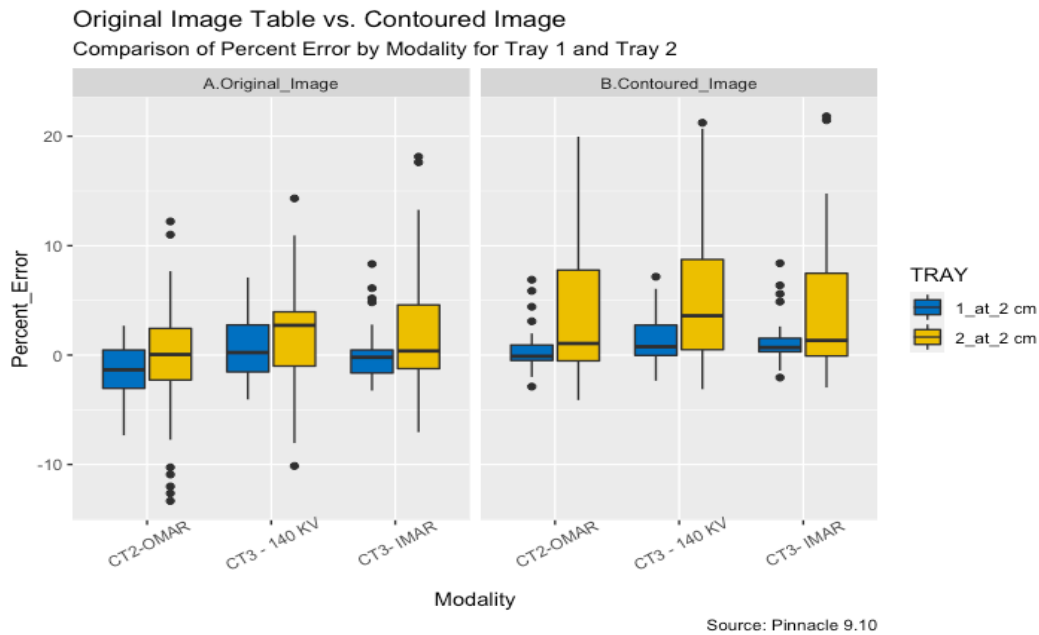


Figure 4.0.15: Percent error distributed for all positions and angles as related to modality for trays, one and two. The left plot shows data from an original scan with MAR correction, while the right plot shows the spread of percent error after applying density overrides for wax and walls.

Percentage error was determined for the gantry at 0° for trays one and two. For tray one, the effect of overriding density was noticeable for CT2-OMAR and CT3-140KV, but minimal for the CT3-IMAR image dataset. This is expected since CT2-OMAR had the most streaking artifacts while CT3-140KV had larger cupping artifacts. Similarly, for tray two with the gantry at 0° , errors increased significantly due to the removal of streaking artifacts. For measurements with the gantry at 180° , removal of the streak artifacts generally improved the results for both trays.

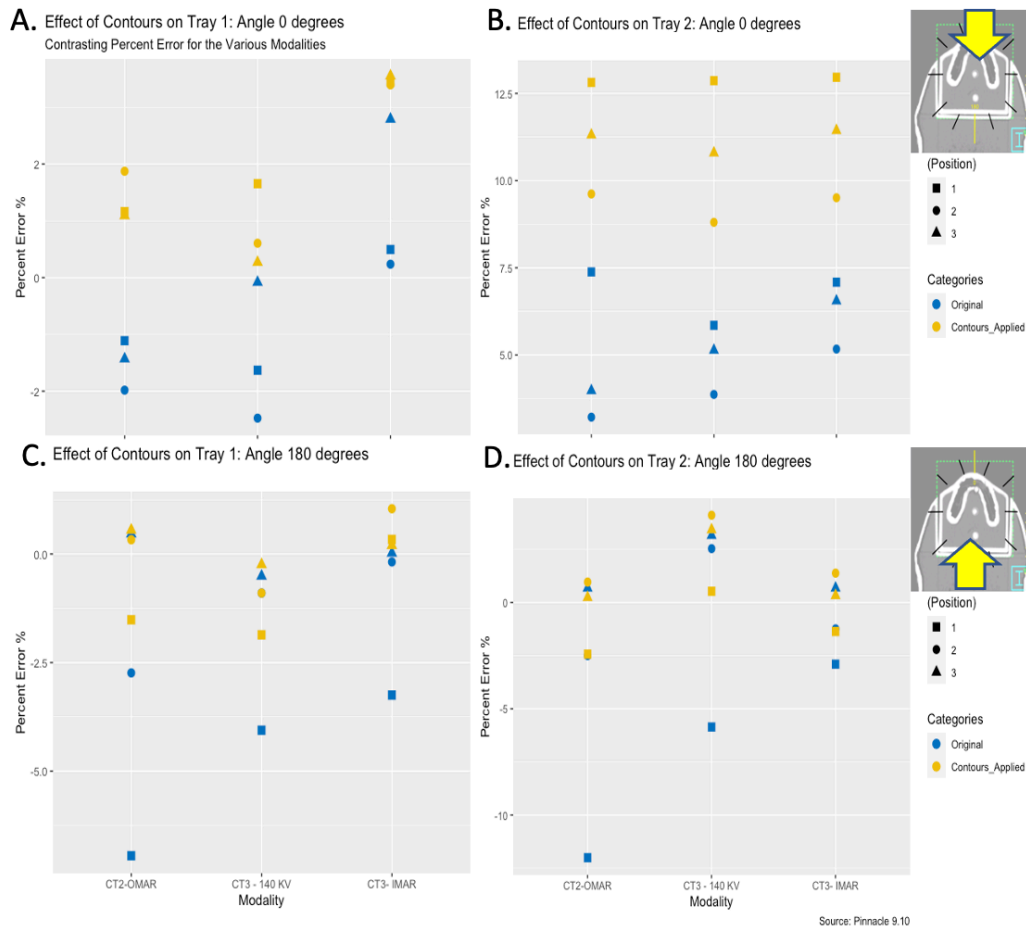


Figure 4.0.16: Percent error plotted as a function of modality for tray one and two for the gantry at 0° and 180° . Shapes indicate positions 1-3. Categories are denoted by colour. Note that readings were taken at 2cm from the base of the phantom in the region consisting of major artifacts from both trays.

The effect of overriding walls and wax was further investigated for the gantry at 45° , and similar results were observed as tray one gantry at 0° . For tray two, gantry at 45° , the percent error significantly increased for position 3 (yellow triangle) as it was located behind a gold implant. A similar effect was observed for position 1 (yellow squares) which was located behind amalgam. In contrast, position 2 (yellow circle) had the slightest positive percent increase due to its location in the direct

path of the beam. Tray two with the gantry at 135° followed similar patterns as gantry at 45°, where position 1 located behind gold (yellow squares) had a significant positive percent (%) increase compared to the original calculation (blue squares). Findings for positions 2 and 3 however showed minimal improvement due to their position in the direct path of the beam. Similarly, for tray one, the gantry at 135° had identical outcomes as gantry at 45°.

In summary, applying density overrides for wall and wax produced a small positive percent error for all gantry angles in tray one and decreased percent error for beams not passing through dental work for tray two.

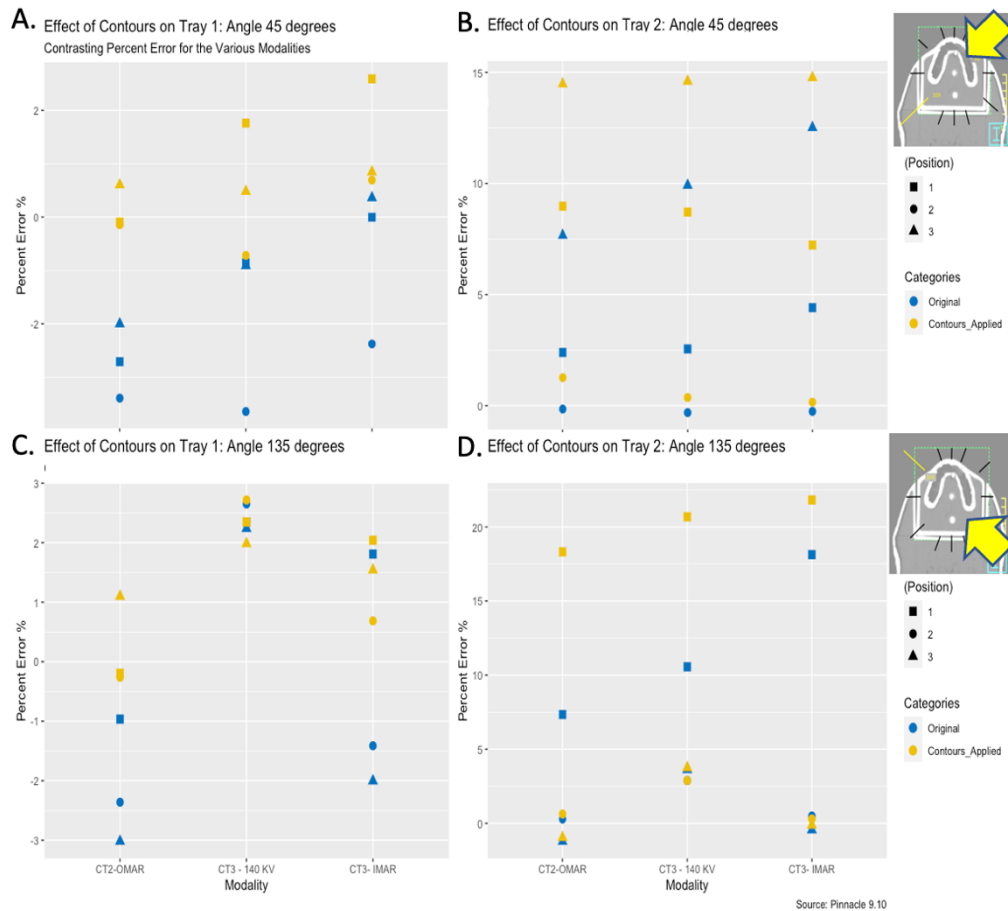


Figure 4.0.17: Percent error as a function of modality for trays one and two for gantry at 45° and 135° . Shapes indicate positions 1-3. Categories are denoted by colour. Note that readings were taken at 2cm from the base of the phantom in the region consisting of major artifacts for both trays.

4.0.4 Effective Density Determination

Figure 4.0.18 shows the CT image of the same representative slice with artifacts and the manual density overrides of walls and wax. Insertion of effective density along with overrides of walls and wax is seen in Figure 4.0.18B for only the MAR reconstructed image data sets. The saturation region did not remain the same for the

MVCBCT image as for the MAR CT image sets, however, the differences appeared to be minor and were considered negligible as they were overridden with the contours of walls and wax. Percent error was calculated after effective density was determined and overrides applied. The change in the distribution was observed in comparison to the original data.

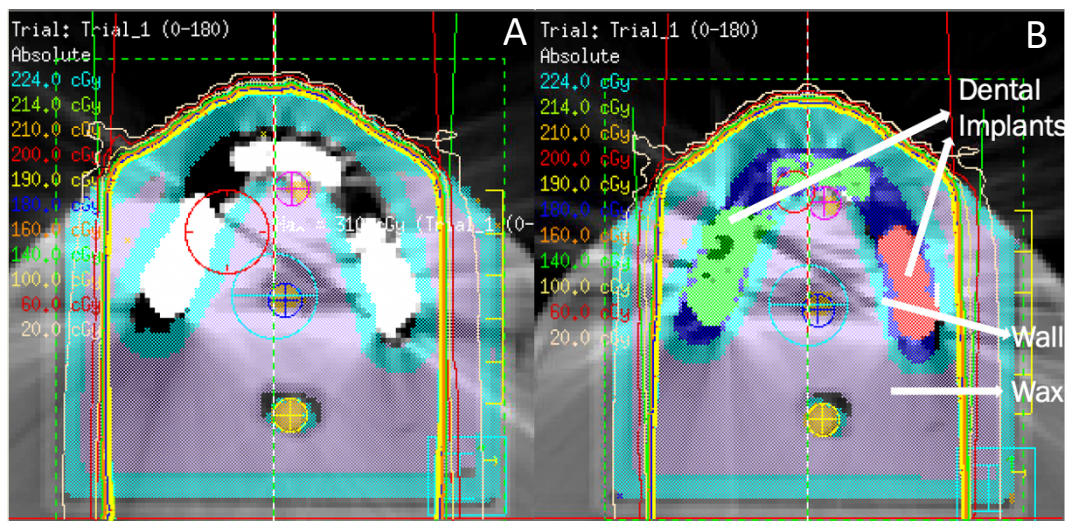


Figure 4.0.18: Image shows axial OMAR reconstructed CT image for (A) tray one with the addition of manual density overrides of walls and wax and the (B) further addition of manual density overrides of effective density.

Overriding a region of saturated pixels with the density of the actual material may be problematic since the saturated region does not correspond to the shape of the implant. In fact, the saturated region is generally larger in dimension by a scale factor. If the true density of the implant is $\rho_{implant}$ and the true distance a beam traverses the implant is $x_{implant}$, then an effective density, $\rho_{effective}$ can be assigned to the saturated pixels corresponding to the implant that compensates for the distance, $x_{effective}$, that a beam traverses through the saturated pixels.

Therefore, to preserve the radiological path length through the implant represented in the CT scan, we require:

$$\rho_{implant} \cdot x_{implant} = \rho_{effective} \cdot x_{effective} \quad (\text{Eq. 4.1})$$

The distance through saturated pixels, $x_{effective}$ is assigned a scale factor, s , of the true distance through the implant, $x_{implant}$.

$$x_{effective} = s \cdot x_{implant} \quad (\text{Eq. 4.2})$$

The effective density of the material needed to give the same attenuation as if the material was correctly represented in the CT scan can be found with the equation:

$$\rho_{implant} \cdot x_{implant} = \rho_{effective} \cdot x_{effective} = \rho_{effective} \cdot s \cdot x_{implant} \quad (\text{Eq. 4.3})$$

Therefore, the effective density of the material is:

$$\rho_{effective} = \frac{1}{s} \times \rho_{implant} \quad (\text{Eq. 4.4})$$

The distance through saturated pixels, $x_{effective}$ is assumed to be roughly twice the size of $x_{implant}$ for high density materials. Hence, the scale factor, s , is substituted by two and the effective density is estimated to be half the true density. For a 6MV

photon beam, amalgam has a density of $\rho = 8 \text{ g/cm}^3$. Therefore, values were substituted, and the effective density of the sample, amalgam, was found from the equation to be $\approx 4 \text{ g/cm}^3$. The same was done to determine an effective density for gold and Co-Cr-Mo alloy. These densities are known as calculated density.

Figure 4.0.19A compares the percent error with no overrides to percent error when saturation regions are overridden with physical, calculated, and low densities for tray two with the gantry at 0° and the detector at position 1. Using the physical density (navy blue) results in large negative errors when compared to all other instances. A similar consequence of using physical density (amalgam = 8 g/cm^3 and gold = 19.2 g/cm^3) was further seen for tray two, with the gantry at 90° and the detector at position 2. Results in Figure 4.0.19 B indicate that in contrast to the positive percent error seen for the gantry at 0° (red), the gantry at 90° (red) showed a negative percent error for calculated density (amalgam = 4 g/cm^3 and gold = 9.5 g/cm^3). Additionally, percent error for a low density (amalgam = 3 g/cm^3 and gold = 4 g/cm^3) was calculated and excessive positive errors were seen for both trays, with tray two having double the percent error to tray one. Therefore, a compromise was attempted using trial and error for a more effective density for both implants.

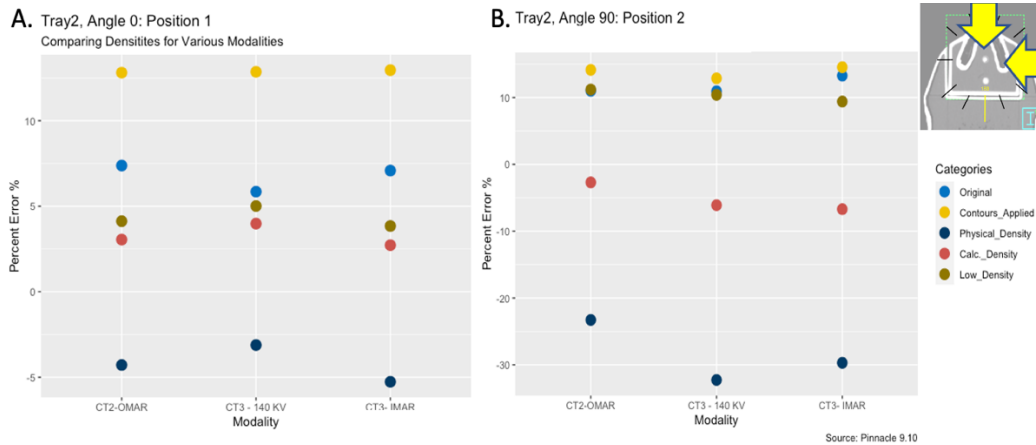


Figure 4.0.19: Percent error plotted as a function of modality for tray two with the gantry at 0° , for positions, 1 and 2. Categories are indicated by colour with five distinctions: original data (blue), data after density overrides of walls and wax (yellow), density overrides of walls, wax, and physical density (navy blue), density overrides of walls, wax, and calculated density (red) and density overrides of walls, wax, and low density (mustard).

A compromise was achieved using a more effective density of amalgam = 5.5 g/cm^3 and gold = 6.5 g/cm^3 . The outcome of applying effective density is shown in Figure 4.0.20, which shows the percent error from the initial uncorrected data sets compared to the manually corrected image sets with density overrides of wall wax and effective density. In all cases, the effective density (grey) results in the smallest errors. This is also the case for the gantry at 15° , 165° , 195° , 225° , 315° and 345° . Therefore, the effective density was deemed the most accurate for regions of dental implants in tray two. This analysis was repeated for gantry at 180° as the beam does not pass through dental implants. The change in percent error for data after the override of walls and wax was negligible. This can be seen in Figure 4.0.21, where the percent error does not change after the density was overwritten in the contour of walls and wax.

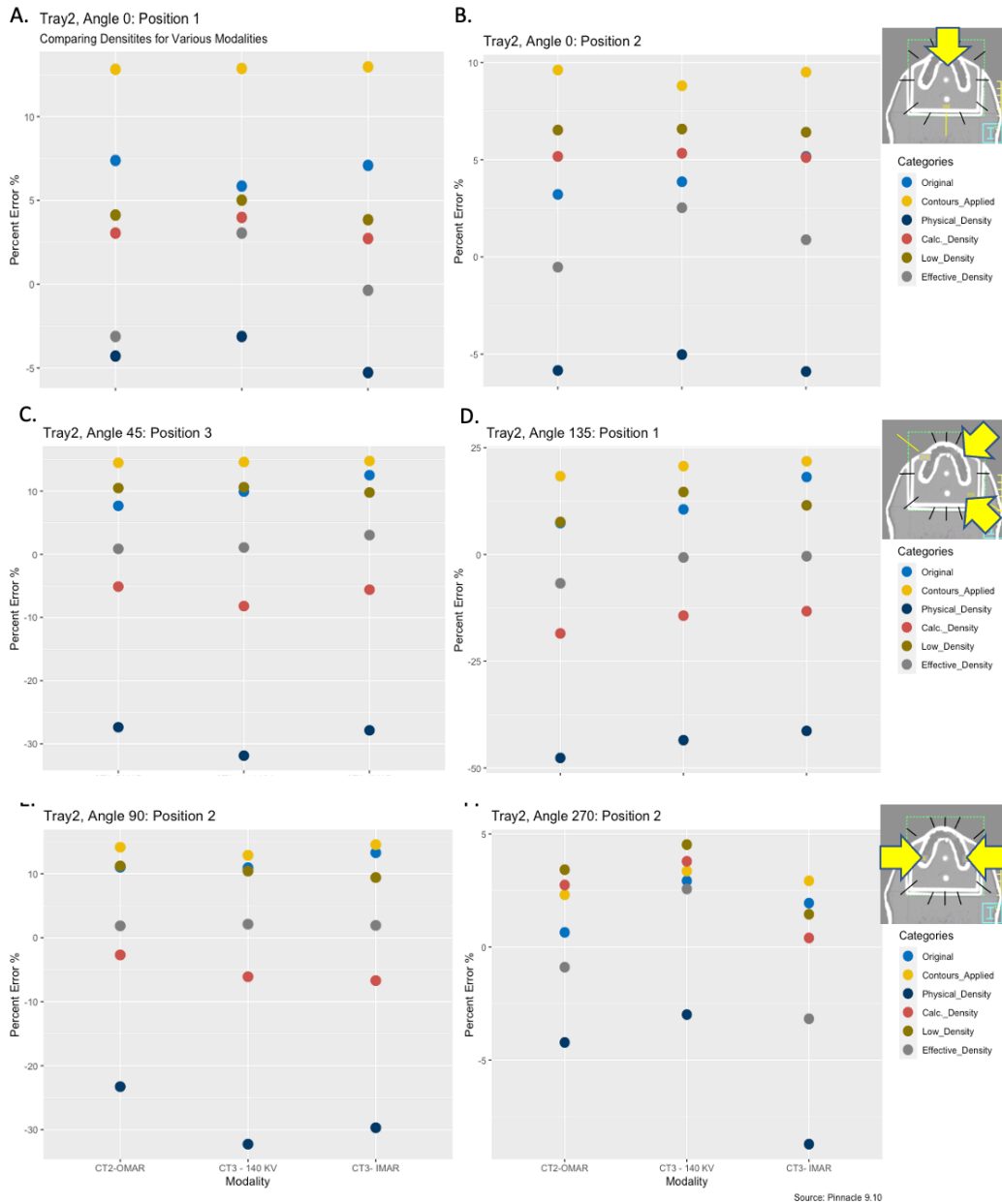


Figure 4.0.20: Percent error plotted as a function of modality for tray two at A) beam angle 0° , for position 1, B) beam angle 0° , for position 2, C) beam angle 45° , at position 3, D) angle 135° , at position 1, E) angle 90° , at position 2 and F) angle 270° , for position 2. Categories are indicated by colour with six distinctions: original data (blue), data after density overrides of walls and wax (yellow), density overrides of walls, wax, and physical density (navy blue), density overrides of walls, wax, and calculated density (red), density overrides of walls, wax, and low density (mustard) and density overrides of walls, wax, and effective density (grey).

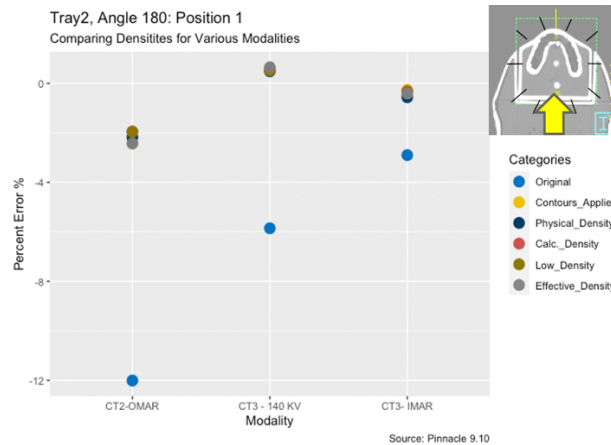


Figure 4.0.21: Percent error plotted as a function of modality for tray two with the gantry at 180° for position one. The graph shows that changes in density overrides; *Physical_Density*, *Calc_Density*, *Low_Density* and *Effective_Density*, have a negligible effect on dose calculations. *Contours_Applied*, *Physical_Density*, *Calc_Density*, *Low_Density* and *Effective_Density* overlap as percent error does not change, hence, only *Effective_Density* is visible.

Figure 4.0.22 A compares the percent error with no overrides to percent error when saturation regions are overridden with physical, calculated, high and effective densities for tray one with the gantry at 0° and the detector at position 1. Using the physical density of amalgam = 8 g/cm^3 and Co-Cr-Mo = 7.9 g/cm^3 (navy blue) results in large negative errors when compared to all other instances. Additionally, percent error for a high calculated density (amalgam = 5 g/cm^3 and Co-Cr-Mo = 5 g/cm^3) was determined and a reduction was seen in negative percent errors for tray one. Recall in Figure. 4.0.19, low density (amalgam = 3 g/cm^3) gave a positive percent error for amalgam. A compromise was attempted using trial and error for a more effective density for both implants (amalgam = 4.5 g/cm^3 , Co-Cr-Mo = 4.5 g/cm^3). Table 4.0.1 shows a summary of all densities used in overrides. In most cases, the effective density (grey) results in the smallest errors. This is also the case

for the gantry at 15°, 165°, 195°, 225°, 315° and 345°. Therefore, the effective density was deemed the most accurate for regions of dental implants in tray one. The analysis was repeated for gantry at 180° as the beam does not pass-through dental implants. Like tray two the change in percent error for data after the override of walls and wax was negligible. This can be seen in Figure 4.0.22B, where the percent error does not change after the density was overwritten in the contour of walls and wax.

Type of Density	Amalgam (g/cm ³)	Gold (g/cm ³)	Co-Cr-Mo (g/cm ³)
Physical	8	19.2	7.9
Calculated	4	9.5	4
Low	3	4	-
High	5	-	5
Effective (Tray 1)	4.5	-	4.5
Effective (Tray 2)	5.5	6.5	-

Table 4.0.1: Summary of values used in density overrides of implants.

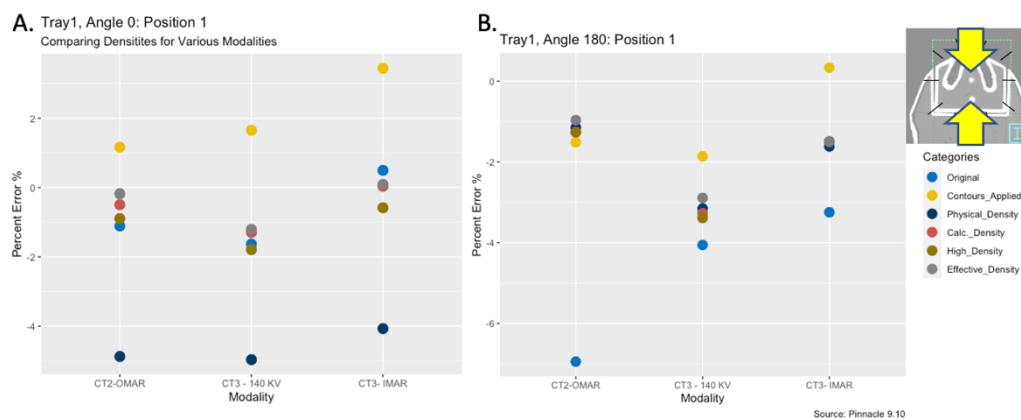


Figure 4.0.22: Percent error plotted as a function of modality for tray one at beam angles 0 and 180, for position 1. Categories are indicated by colour with six distinctions: original data (blue), data after density overrides of walls and wax (yellow), density overrides of walls, wax, and physical density (navy blue), density overrides of walls, wax, and calculated density (red), density overrides of walls, wax, and high density (mustard) and density overrides of walls, wax, and effective density (grey).

4.0.5 Final Results

The final data for tray one in Figure 4.0.23 shows small improvements in percent error compared to the initial data. The range of errors in the initial data were already small, therefore changes appear small in contrast. Nevertheless, the final boxplots are more diminutive, i.e., reflecting that the final percent error is in better agreement than the initial percent error. Whiskers for the final data are also shorter than the initial data. Therefore, using manual overrides of walls, wax, and the effective density of 4.5 g/cm^3 for the implants in the tray one gives consistently stable results within $\pm 4.7\%$ this is less than clinically acceptable uncertainty of $\pm 5\%$ for dose delivery to a target in radiotherapy. Additionally, the boxplot for CT3-IMAR gave the best results with the median at approximately zero and the inter-quartile range less than $\pm 1.5\%$. Therefore CT3-IMAR reconstructed is recommended for situations where the dental implant materials have densities smaller than 10 g/cm^3 , which was found in tray one.

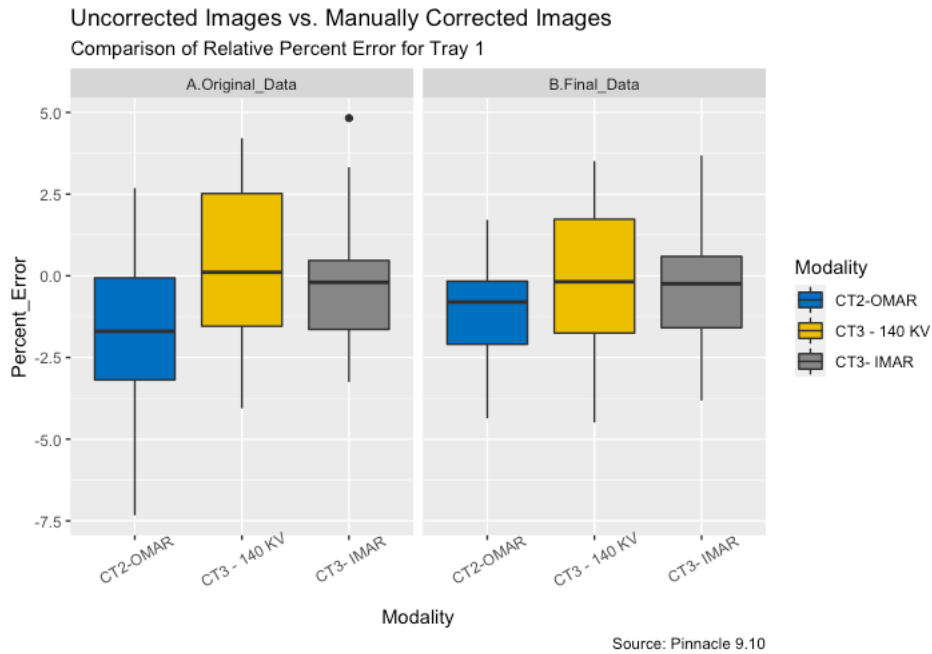


Figure 4.0.23: Comparison of relative percent error for tray one when density overrides of walls and wax are used and when they are not used.

The final data for tray two, Figure 4.0.24 shows an overall tendency for calculated dose to be greater than measured dose. The boxplot for CT2-OMAR produced results with the median at approximately zero and the inter-quartile range less than $\pm 1\%$. However, the boxplot for CT3-IMAR had similar results within 0.5% and fewer outliers. Therefore, it is challenging to state which modality may be best for a reduction in calculation errors and should therefore be left to the physicians' discretion. Whiskers were also relatively short, with fewer outliers compared to the initial data for all modalities. Final percent errors were less than half those of the initial data when an effective density (amalgam = 5.5 g/cm^3 and gold = 6.5 g/cm^3) was used.

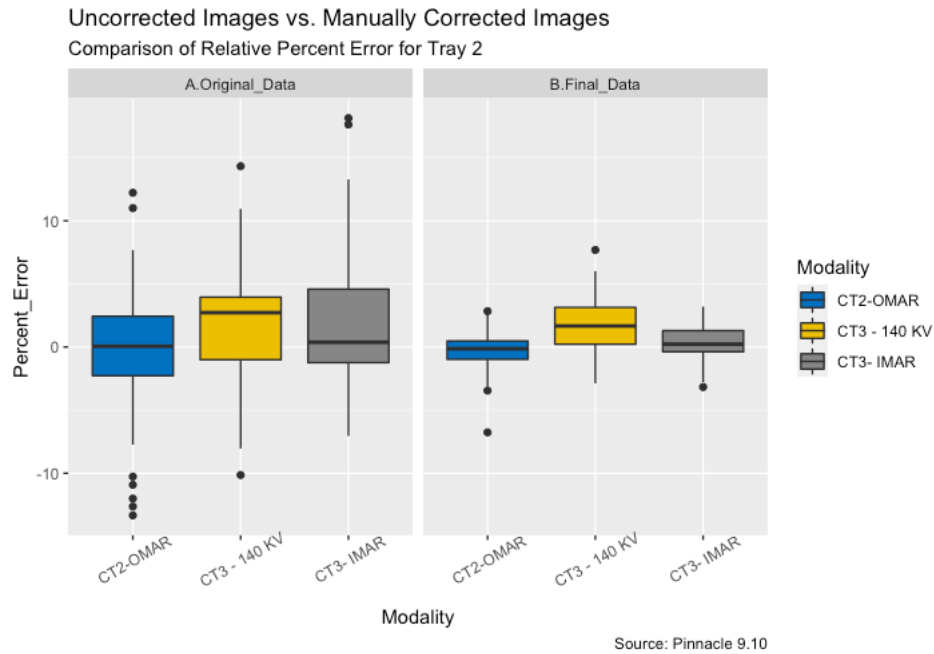


Figure 4.0.24: Comparison of relative percent error for tray two when density overrides of walls, wax, and effective density were used to that when they were not.

In summary, results indicate that the initial dose calculation errors are similar for both MAR reconstructed and uncorrected images, as also determined by Sillanpaa *et al.* and Long *et al.* [3, 11]. Therefore, the study could not firmly state that MAR reconstruction images were more accurate than uncorrected images in all instances. Results did confirm, however, that percent errors are characteristic of artifacts. Furthermore, points of interest closer to dental implants show a more significant disparity between calculated and measured doses. However, differences in dose decreased with an increase in distance away from implants. This was confirmed with the comparison between errors for tray one at 2 cm from the base of the phantom to tray one at 2.3 cm from the base of the phantom. Additionally, it was

determined that the CT number to density table for the head had little effect on the results, so the reference table was used.

Results from data after density overrides of walls and wax were applied indicate that density overrides for regions of known density should be practiced and thus remain in current protocols. Nevertheless, care should be taken when applying this protocol as there may be instances where applying contours results in a more significant percent error due to high calculated doses. High calculated doses in the presence of high-density materials are seen in the study by Shimamoto *et al.* that discovered a dose increase of up to 19% for gold among seven other materials [21]. Density overrides of effective density (amalgam- 4.5g/cm^3 and Co-Cr-Mo- 4.5g/cm^3) for tray one gave the best results in most cases where beams pass through implants. Density overrides of effective density after overriding density in the contours of walls and wax was deemed unnecessary for targets before an implant as the modelled beams do not pass through saturated pixels and therefore have no effect on percent error. Meanwhile, it was determined that overriding nearby regions of artifacts with effective density have little effect on beams not passing through the artifact. In the presence of high density, such as gold in tray two, density overrides of the dental implants are necessary as the volume of saturated pixels are significant. Therefore, for this study, amalgam was found to have an effective density of 5.5g/cm^3 , while gold was found to have an effective density of 6.5g/cm^3 . Using these values for overriding the density of saturated pixels gave the best

agreement with measurements whereby the variation in the clustered percent error was reduced by half compared to that obtained when no overrides were used.

CHAPTER 5

CONCLUSION

This thesis incorporated the use of a dental phantom that simulated a human jaw containing samples of dental work located in the front incisors of the mouth and the left and right molars for both interchangeable dental trays. CT stimulation of the phantom allowed for treatment planning where the dose was calculated. Ion chamber inserts in the dental trays permitted the determination of measured dose by setting up identical couch positions and beams settings as created in the treatment planning system.

Percent error was then determined by finding the difference between calculated and measured doses. This parameter was used throughout the study to establish the influence of image artifacts and, in turn, observe the effect of methods used to reduce the appearance of artifacts and their impact on dose. Results from the study suggested that the percent error is improved after applying density overrides of the known region such as walls and wax of the phantom. Small errors were found in instances where the modelled beam did not pass-through dental work. The use of an effective density for clipped CT pixels was also investigated. An effective density of 4.5 g/cm^3 was determined for amalgam and Co-Cr-Mo alloy in tray one, however in the presence of gold a greater effective density of 5.5 g/cm^3 for amalgam and 6.5 g/cm^3 for gold was calculated.

Meanwhile, despite constant comparison between modalities in the study, conclusions were unable to be made about the most appropriate machine for mitigation of metal artifacts; however, the use of 140 kVp CT acquisition was deemed inadequate.

5.0.2 Limitations

Samples were received from a nearby dentist, and the composition of the implants was unknown. While this was not a significant issue as incidents may arise where a patient is unaware of the exact makeup of their dental work, difficulties arose in distinguishing between Co-Cr-Mo alloy and stainless-steel implants as they have similar density and colour. Therefore, it was assumed that the material was Co-Cr-Mo alloy despite the possibility of being stainless steel for efficiency, as it was anticipated that both materials would yield the similar outcome. Additionally, the effect of DECT combined spectral images was not investigated as the function to merge low and high-energy spectra images on the CT machine was unavailable for this study. Hence, only the 140 kVp energy images were utilized. Results implied that this technique, while reducing the appearance of artifacts, did not improve dose calculation and should not be used in the treatment of patients as benefits do not outweigh the risks.

5.0.4 Considerations

Density overrides of the effective density for the two trays differ by 1 g/cm³ (4.5 g/cm³ and 5.5 g/cm³ for tray one and two respectively) due to gold in tray two. Findings determined that the use of an effective density for amalgam and other materials with density below 10 g/cm³ decreased the discrepancy between measured and calculated doses by a lesser degree compared to the instance with Gold. These results should be further investigated in an effort to discover a single density value for a material that will work for all instances to give the most accurate dose calculations. Therefore, before implementation of the protocol in a clinical setting, scatter doses should be measured by placing radiochromic films behind the metals within the dental cavity. After irradiation the films would then be scanned over a few hours and the dose profile data at the set position would be obtained and available for comparison with measured dose. The use of radiochromic films should be able to produce a clear picture of the dose distribution for Amalgam in the presence of Gold and without Gold. However, this can only be done with the same implant or implants with the same known composition for consistency.

5.0.3 Moving Forward

Results from the comparison of CT density tables for the head geometry to the reference was inconclusive however, during this process, it was observed that the CT number for large densities above 8 g/cm³ such as gold was estimated by

extrapolation of the table to a density of 20 g/cm³. It would be worthwhile to explore the effect of the CT to density table beyond the CT# saturation region as it grossly extrapolated and therefore very uncertain. On the other hand, if density is overridden directly (as opposed to overriding CT#, then one might like to be sure whether the table has any relevance to the outcome of the calculation. Furthermore, a table listing all known materials of dental prostheses can be created for quick access to the effective densities of each compound. The utilization of MVCBCT images for better visualization of dental work may also be implemented. This can be done by acquiring the MVCBCT images during the first treatment of the patient and using the image data sets in re-evaluation plans for contours. This approach would allow for the use of effective densities that are much closer to the actual densities of the implants as the implant geometry represented in the image approaches that of the actual implant.

Machine Learning can also be a solution to the current planning process. MVCBCT images greatly reduce the appearance of artifacts which aids in creating contours. Programs would be employed that reconstruct the artifact-plagued image based on the predictive learning from the kVCT/MVCBCT image sets. Hence, a neural network can be trained to recognize the CT artifact patterns caused by specific dental implants [25]. The success of such programs will allow for accurate contours of implants and tissue, improve dose calculation, and increase the efficiency of the radiation therapy treatment planning process to increase accuracy while shortening time. Additionally, this study was limited to head and neck

cancers, where dental prostheses are small in nature and produce errors in dose calculation reflective of size. The implication for larger implants may be studied using similar methods to determine the influence on dose calculation errors in surrounding healthy tissue and the effect mitigation techniques would have on these errors.

5.0.4 Conclusion

Overall, the study has revealed that normal tissue doses are not significantly affected by metal artifact reduction (MAR) algorithms, as the difference compared to uncorrected CT images is small. Cases will vary for each individual, and the modes available for CT simulation is at the sole discretion of the physician.

Head and Neck cancer patients experience side effects that affect their quality of life, such as damage to salivary glands, which may cause dryness in the mouth, a change in taste leading to a reduced appetite and pain/ irritation (swelling, mouth sores and sore throat). Evidence led to the deduction that manual overrides of effective density in addition to density overrides of known density can be useful in reducing the uncertainty in dose calculations in the treatment planning system. This is especially true for instances where gold is present. Patients with implants such as amalgam may be currently receiving a slightly lower dose to surrounding healthy tissue without the implementation of effective density, since the beam will be more attenuated in the patient than is accounted for in the plan. Furthermore, the inclusion

of a MVCBCT image set can improve implant visualization which can reduce the treatment planning time as there is less uncertainty when having to contour image artifacts. Note that the saturation region did not remain the same for the MVCBCT image as for the MAR CT image sets, however, the differences appeared to be minor and were considered negligible as they were overridden with walls and wax.

Implementation of these process improvements, continuous monitoring and further modification of processes will succeed in achieving a more efficient treatment planning protocol while simultaneously improving dose calculation toward a superior quality of care.

BIBLIOGRAPHY

- [1] Canadian Cancer Society , "Oral Cavity Cancer Statistics," 2021. [Online]. Available: <https://www.cancer.ca/en/cancer-information/cancer-type/oral/statistics/?region=on>. [Accessed August 2021].
- [2] McMaster University, "Department of Surgery - Specialty Clinics," 2017. [Online]. Available: <https://surgery.mcmaster.ca/divisions/otolaryngology-head-and-neck-surgery/specialty-clinics/cancer-clinics>. [Accessed August 2021].
- [3] J. Sillanpaa, M. Lovelock and B. Mueller, "The effects of the orthopedic metal artifact reduction (O-MAR) algorithm on contouring and dosimetry of head and neck," *Medical Dosimetry*, vol. 45, no. 1, pp. 92-96, 2020.
- [4] M. Azizi, A. A. Mowlavi, M. Ghorhani, B. Azadegan and F. Akbari, "Dosimetric evaluation of scattered and attenuated radiation due to dental restorations in head and neck radiotherapy," *Journal of Radiation Research and Applied Sciences*, vol. 11, no. 1, pp. 23-28, 2018.
- [5] C. De Conto, R. Gschwind, E. Martin and L. Makovicka, "Physica Medica," *Study of dental protheses influence in radiation therapy*, vol. 30, no. 1, pp. 117-121, 2014.
- [6] J. F. Barrett and N. Keat, "Artifacts in CT: Recognition and Avoidance," *Radiographics*, vol. 24, no. 6, pp. 1679-1691, 2004.
- [7] M. Katsura, J. Sato, M. Akahane, A. Kunimatsu and O. Abe, "Current and novel techniques for metal artifact reduction at CT: Practical guide for radiologists," *Radiographics*, vol. 38, no. 2, pp. 450-461, 2018.
- [8] C. Ziemann, M. Stille, F. Cremers, T. M. Buzug and D. Rades, "Improvement of dose calculation in radiation therapy due to metal artifact correction using the augmented likelihood image reconstruction," *Journal of Applied Clinical Medical Physics*, vol. 19, no. 3, pp. 227-233, 2018.
- [9] K. M. Andersson, P. Nowik, J. Persliden, P. Thunberg and E. Norman, "Metal artefact reduction in CT imaging of hip protheses - an evaluation of commercial techniques provided by four vendors," *British Journal of Radiology*, vol. 88, no. 1052, 2015.
- [10] D. Zhang and E. Angel, "Single Energy Metal Artifact Reduction A Reliable Metal Mangement Tool in CT," Toshiba America Medical Systems, Inc., Tustin, 2017.
- [11] Z. Long, M. R. Bruesewitz, D. R. DeLone, J. M. Morris, K. K. Amrami, M. C. Adkins, K. N. Glazebrook, J. M. Kofler, S. Leng, C. H. McCollough, J. G. Fletcher, A. F. Halaweish and L. Yu, "Evaluation of projection - and dual-energy based methods for metal artifact reduction in CT using a phantom study," *Journal of Applied Clinical Medical Physics*, vol. 19, no. 4, 2018.

- [12] R. Ghasemi Shayan, M. Oladghaffari, F. Sajjadian and M. Fazel Ghaziyani, "Image Quality and Dose Comparison of Single-Energy CT (SECT) and Dual-Energy CT (DECT)," *Radiology Research and Practice*, vol. 2020, pp. 1-11, 2020.
- [13] F. Sterzing, J. Kalz, G. Sroka-Perez, K. Schubert, M. Bischof, F. Roder, J. Debus and K. Herfarth, "Megavoltage CT in Helical Tomotherapy- Clinical Advantages and Limitations of Special Physical Characteristics," *Technology in Cancer Research and Treatment*, vol. 8, no. 5, October 2009.
- [14] J. L. Schreiner, M. Rogers, G. Salomons and A. Kerr, "Metal artifact suppression in megavoltage computed tomography," in *Proceedings of the SPIE*, California, 2005.
- [15] D. Chapman, S. Smith, R. Barnett, G. Bauman and S. Yartsev, "Optimization of tomotherapy treatment planning for patients with bilateral hip prostheses," *Radiation Oncology*, vol. 9, no. 1, 2014.
- [16] M. F. Spadea, J. Verburg, G. Baroni and J. Seco, "Dosimetric assessment of a novel metal artifact reduction method in CT images," *Journal of Applied Clinical Medical Physics*, vol. 14, no. 1, pp. 299-304, 2013.
- [17] T. Razi, M. Niknami and F. Alavi Ghazani, "Relationship between Hounsfield Unit in CT Scan and Gray Scale in CBCT," *Journal of dental research, dental clinics, dental prospects*, vol. 8, no. 2, pp. 107-110, 2014.
- [18] T. Razi, P. Emamverdzadeh, N. Nilavar and S. Razi, "Comparison of the Hounsfield Unit in CT scan with the Gray Level in cone-beam CT," *Journal of Dental Research, Dental Clinics, Dental Prospects*, vol. 13, no. 3, pp. 177-182, 2019.
- [19] C. Levi, J. E. Gray, E. C. McCullough and R. R. Hattery, "The unreliability of CT numbers as absolute values," *American Journal of Roentgenology*, vol. 139, no. 3, 1982.
- [20] D. Fornell, "An Introduction to Current Radiation Therapy Treatment Planning Systems," *Imaging Technology News*, 8 July 2013.
- [21] H. Shimamoto, I. Sumida, N. Kakimoto, K. Marutani, R. Okahata, A. Usami, T. Tsujimoto, S. Murakami, S. Furukawa and S. Tetradis, "Evaluation of the scatter doses in the direction of the buccal mucosa from dental metals," vol. 16, no. 3, pp. 233-243, 2015.
- [22] C. R. Hansen, R. L. Christiansen, E. L. Lorenzen, A. S. Bertelsen, J. T. Asmussen, N. Gyldenkerme, J. G. Eriksen, J. Johansen and C. Brink, "Contouring and dose calculation in head and neck cancer radiotherapy after reduction of metal artifacts in CT images," *Acta Oncologica*, vol. 56, no. 6, pp. 874-878, 2017.
- [23] M. Hagen, M. Kretschmer, F. Wurschmidt, T. Gauer, C. Giro, E. Karsten and J. Lorenzen, "Clinical relevance of metal artefact reduction in computed tomography (iMAR) in the pelvic and head and neck region: Multi-

- institutional contouring study of gross tumour volumes and organs at risk on clinical cases," *Journal of Medical Imaging and Radiation Oncology*, vol. 63, no. 6, pp. 842-851, 2019.
- [24] P. R. Almond, P. J. Biggs, B. M. Coursey, W. F. Hanson, S. M. Huq, R. Nath and D. W. O. Rogers, "AAPM's TG-51 protocol for clinical reference dosimetry of high energy photon and electron beams," 1999.
- [25] L. Hyunkwang, H. Chao, Y. Sehyo, T. H. Shahein, K. Myeongchan and D. Synho, "Machine Friendly Machine Learning: Interpretation of Computed Tomography Without Image Reconstruction," *Scientific Reports*, vol. 9, no. 1, 2019.
- [26] N. Agazaryan, P. Chow, J. Lamb, M. Cao, A. Raldow, P. Beron, J. Hegde and M. Steinberg, "The Timeless Initiative: Continuous Process Improvement for Prompt Initiation of Radiation Therapy Treatment," *Advances in Radiation Oncology*, vol. 5, no. 5, pp. 1014-1021, 2020.
- [27] Z. Xu, R. Yao, M. B. Podgorsak and I. Z. Wang, "Effects of collimator angle, couch angle and starting phase on motion-tracking dynamic conformal arc therapy (4D DCAT)," *Journal of Applied Clinical Medical Physics*, vol. 18, no. 5, pp. 54-63, 2017.

APPENDIX A

Appendix A.1: Tray one, Additional Results After Density Overrides in the Contours



Figure A.1: Percent error plotted as a function of modality for tray one, comparing original data to results after overriding density in the contours of walls and wax.

Appendix A.2: Tray two, Additional Results After Density Overrides in the Contours

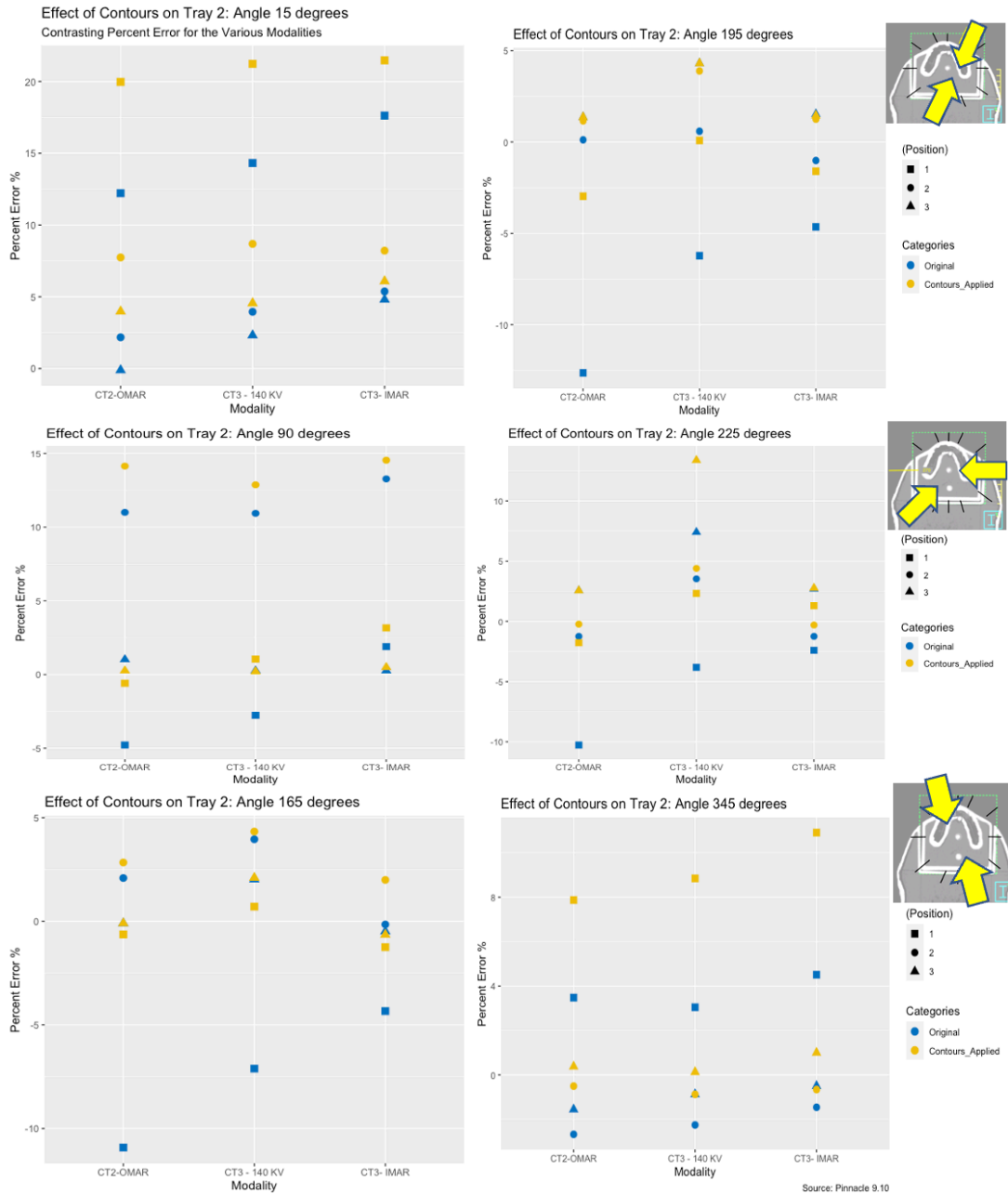


Figure A.2: Percent error plotted as a function of modality for tray two, comparing original data to results after overriding density in the contours of walls and wax.

Appendix A.3: Tray one, Additional Results After Density Overrides of Effective Density



Figure A.3: Percent error plotted as a function of modality for tray one, comparing the influence of the various density overrides to the original results. In some cases, Contours_Applied, Physical_Density, Calc_Density, High_Density and Effective_Density overlap as percent error does not change.

Appendix A.4: Tray two, Additional Results After Density Overrides of Effective Density



Figure A.4: Percent error plotted as a function of modality for tray two, comparing the influence of the various density overrides to the original results. In some cases, Contours_Applied, Physical_Density, Calc_Density, Low_Density and Effective_Density overlap as percent error does not change.